

# **EVALUATING LONG-TERM SHORELINE CHANGE IN DAKAR (SENEGAL) USING SATELLITE DATA**

PAUL NGOZI OJUKWU

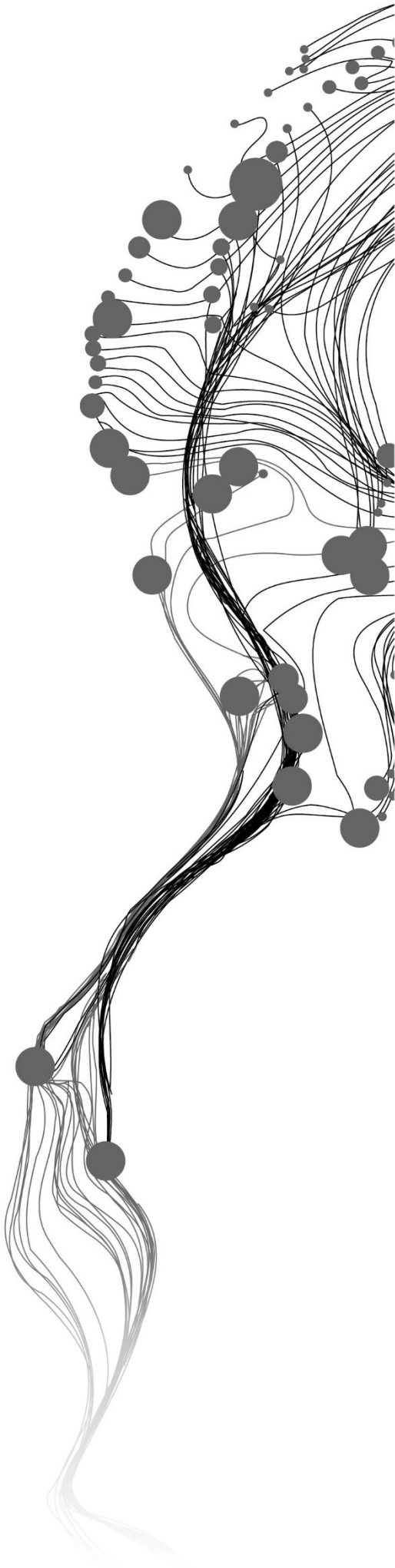
June, 2021

SUPERVISORS:

Dr. ir. S. Salama

Prof. Dr. D. van der Wal





# **EVALUATING LONG-TERM SHORELINE CHANGE IN DAKAR (SENEGAL) USING SATELLITE DATA**

**PAUL NGOZI OJUKWU**

Enschede, The Netherlands, June 2021

Thesis submitted to the Faculty of Geo-Information Science and Earth Observation of the University of Twente in partial fulfilment of the requirements for the degree of Master of Science in Geo-information Science and Earth Observation.

Specialization: Water Resources and Environmental Management

**SUPERVISORS:**

Dr. ir. S. Salama

Prof. Dr. D. van der Wal

**THESIS ASSESSMENT BOARD:**

Dr. ir. C. M. M. Mannaerts (Chair)

Prof. C. Gommenginger (External Examiner, National Oceanography Centre)

#### DISCLAIMER

This document describes work undertaken as part of a programme of study at the Faculty of Geo-Information Science and Earth Observation of the University of Twente. All views and opinions expressed therein remain the sole responsibility of the author, and do not necessarily represent those of the Faculty.

## ABSTRACT

---

The rate of sea-level rise (SLR) influenced by global warming has increased the risk of coastal flooding. Long-term sea-level rise induces shoreline retreat. Shoreline monitoring is necessary for beach monitoring, identifying areas that are vulnerable to coastal erosion and flooding, and sustainable management of the coastal environment. Remote sensing offers possibilities for regional monitoring and analysis of coastal dynamics in a fast, efficient, and relatively cheap way. This study investigates the long-term shoreline change in Dakar (Senegal) for the past 20 years using satellite data. Shorelines extracted from median composite images of Landsat-7 (ETM+), Landsat-8 (OLI), Sentinel-1 (SAR), and Sentinel-2 (MSI) using Modified Normalized Difference Water Index, adaptive thresholding, and Canny Edge Detection techniques were compared. The change statistics of the extracted shorelines were analysed using the Digital Shoreline Analysis System (DSAS), a software extension in ArcGIS for calculating shoreline change statistics and making forecasts, with the Net Shoreline Movement (NSM) and End Point Rate (EPR) techniques. The DSAS was used to calculate future positions of the shoreline for the next 10 and 20 years (using the Linear Regression Rate (LRR)). Finally, the study explored the influence of sea-level rise on shoreline change and identified areas vulnerable to shoreline retreat. Modified Normalized Difference Water Index (MNDWI) was more reliable in delineating the shoreline than adaptive thresholding and Canny Edge Detection techniques. Validation of the shorelines extracted from satellite data (Landsat 7, Landsat 8, and Sentinel-2) using MNDWI revealed that their positions fell within the high and low waterline. The accuracy assessment returned an overall mean ( $\mu$ ) error of 20.9 m (seaward bias with Root Mean Square Error (RMSE) not exceeding 33.0 m) and -11.9 m (landward bias with RMSE not exceeding 28.6m) with respect to the high and low waterline, respectively. The evolution of the shoreline from 2000 to 2020 reveals an erosive trend with an average Net Shoreline Movement (NSM) and End Point Rate (EPR) of -71.2 m of -3.6 m/year, respectively. The negative correlation obtained between shoreline displacement and increasing sea level provides insight into the potential SLR has on the retreating shoreline. Prediction of the shoreline position in 2100 (considering the high emission scenario (RCP 8.5) of SLR projection ( $> 1$  m by 2100)) using the linear regression model equation obtained linking shoreline displacement and sea-level reveals that the shoreline is likely to retreat by 187.2 m landward from the 2020 shoreline position.

**Keywords:**

**Shoreline, Net Shoreline Movement (NSM), End Point Rate (EPR), Linear Regression Rate (LRR), and Sea level rise (SLR)**

## ACKNOWLEDGEMENTS

---

I dedicate this work to the Almighty God. I give Him all the glory for giving me the grace, strength, and sound mind to complete my study and research.

I am most grateful for the opportunity and scholarship awarded to me by the Dutch Government and the Orange Knowledge Programme (OKP) to pursue this programme at the University of Twente. I am pleased to express my appreciation to the National Space Research and Development Agency in Nigeria for backing me to study abroad. It is heart-warming to have carried out this research in the framework of the European Space Agency (ESA) Earth Observation for Sustainable Development (EO4SD) Marine and Coastal Initiative.

My profound gratitude goes to my supervisors, Dr. ir. S. Salama and Prof. Dr. D. van der Wal. Their guidance, advice, and detailed review of my report enhanced the quality of this thesis.

My sincere appreciation goes to all lecturers and staff members in the Department of Water Resources and Faculty of Geo-information and Earth Observation (ITC) for their assistance and knowledge sharing. I appreciate the encouragement and support I received from my study advisor, Ir. A. M. van Lieshout during my study period.

Special thanks to Stephen Carpenter, Clive Neil, and the entire satellite team at the National Oceanography Centre (United Kingdom) for their support during my internship. My sincere gratitude goes to Dr. ir. R. van der Velde for his guidance and supervision during my internship.

I would like to thank Dr. Moussa Sall and Ousmane Bocoum from the Centre de Suivi Ecologique, and Abdoulaye Ndour and Djibril Tine from Dakar's University for providing the Differential GPS measurements of the Pikine coastal shoreline.

I want to thank my friends in the Department of Water Resources (ITC), ITC, University of Twente, and TU Delft. Interacting with them was helpful during the period of my study.

Finally, my heartfelt gratitude goes to my entire family for their love and support. Keeping in touch and praying for me strengthened me emotionally.

# TABLE OF CONTENTS

---

Abstract .....	i
Acknowledgements .....	ii
List of figures .....	iv
List of tables .....	v
Acronyms.....	vi
<b>1. INTRODUCTION .....</b>	<b>1</b>
1.1. Background .....	1
1.2. Research problem.....	1
1.3. Research justification.....	2
1.4. Research objectives.....	2
1.5. Research questions.....	2
1.6. Study area .....	2
<b>2. CONCEPTUAL FRAMEWORK AND RELATED WORKS .....</b>	<b>4</b>
2.1. Shoreline dynamics and evolution.....	4
2.2. Identification of shoreline indicators .....	4
2.3. Remote sensing application in shoreline extraction .....	5
2.4. Water-land segmentation .....	6
2.5. Literature review.....	10
<b>3. RESEARCH METHODOLOGY .....</b>	<b>11</b>
3.1. Work Flow .....	11
3.2. Data collection.....	11
3.3. Satellite image processing .....	12
3.4. Shoreline extraction .....	13
3.5. Shoreline validation.....	14
3.6. Shoreline evolution .....	14
3.7. Vulnerability assessment of shoreline change .....	15
3.8. Shoreline and sea-level data analysis .....	15
<b>4. RESULTS AND DISCUSSION .....</b>	<b>18</b>
4.1. Results .....	18
4.2. Discussion .....	34
<b>5. CONCLUSION AND RECOMMENDATIONS .....</b>	<b>38</b>
5.1. Conclusion.....	38
5.2. Recommendations .....	38
<b>LIST OF REFERENCES.....</b>	<b>40</b>

## LIST OF FIGURES

---

<b>Figure 1.</b> Study area in Senegal. ....	3
<b>Figure 2.</b> Schematic representation of the spatial relationship between typical shoreline indicators (Source: Boak & Turner (2005)). ....	5
<b>Figure 3.</b> Spatial resolution and spectral range of Landsat (7 and 8) and Sentinel-2 bands (in the optical spectral region) (Source: (Pardo-Pascual et al., 2018)). ....	8
<b>Figure 4.</b> Flowchart of the methodology for the study. ....	11
<b>Figure 5.</b> Overlay of shoreline extracted from 2010 Landsat-7 median composite image using (a) MNDWI (on MNDWI image), (b) adaptive thresholding (on MIR band), (c) MNDWI (on RGB composite image), (d) adaptive thresholding (RGB composite image). ....	18
<b>Figure 6.</b> Overlay of shoreline extracted from 2013 Landsat-8 median composite image using (a) MNDWI (on MNDWI image), (b) adaptive thresholding (on MIR band), (c) MNDWI (on RGB composite image), (d) adaptive thresholding (RGB composite image). ....	19
<b>Figure 7.</b> Overlay of shoreline extracted from 2020 Sentinel-2 median composite image using (a) MNDWI (on MNDWI image), (b) adaptive thresholding (on MIR band), (c) MNDWI (on RGB composite image), (d) adaptive thresholding (RGB composite image). ....	19
<b>Figure 8.</b> Overlay of shoreline extracted from 2020 Sentinel-1 median composite using Canny Edge Detection on (a) 2020 Sentinel-1 median composite image, (b) 2020 Sentinel-2 median composite, (RGB) image. ....	20
<b>Figure 9.</b> Overlay of shorelines extracted from 2020 Sentinel-2 median composite image using Canny Edge Detection on (a) 2020 Sentinel-2 median composite (MIR band), (b) 2020 Sentinel-2 median composite (RGB) image. ....	20
<b>Figure 10.</b> Comparison of shorelines derived from 2020 median composite (01 December 2020 to 31 December 2020) images of Landsat-7, Landsat-8, and Sentinel-2 using MNDWI. ....	21
<b>Figure 11.</b> (a) Histogram of horizontal displacement (along transects) of satellite-derived shorelines from the high waterline (b) boxplot of horizontal displacement (along transects) of satellite-derived shorelines (from different satellite missions) from the high waterline. ....	22
<b>Figure 12.</b> (a) Histogram of horizontal displacement (along transects) of satellite-derived shorelines from the low waterline (b) boxplot of horizontal displacement (along transects) of satellite-derived shorelines (from different satellite missions) from the low waterline. ....	23
<b>Figure 13.</b> Net Shoreline Movement (NSM, in meters) of shorelines from 2000 - 2020 (a) across transects (b) scatter (line) plot. ....	24
<b>Figure 14.</b> Scatter plot showing the Linear Regression Rater (LRR) of the shoreline from 2000 to 2020. ....	25
<b>Figure 15.</b> End Point Rate (EPR, in m/year) of shorelines derived from 2000 – 2020 (a) across transects (b) scatter (line) plot. ....	26
<b>Figure 16.</b> Forecasts (10- and 20-year) of the shoreline position. ....	27
<b>Figure 17.</b> Elevation map covering part of the built-up area close to the shoreline. ....	28
<b>Figure 18.</b> Annual mean sea-level from 2007 to 2020. ....	29
<b>Figure 19.</b> Annual maximum sea-level from 2007 to 2020. ....	29
<b>Figure 20.</b> Scatter plot of annual mean shoreline displacement (m) and annual maximum sea-level (mm) ....	34
<b>Figure 21.</b> Active profile response to sea-level rise according to the Bruun rule (Source: (Dean & Houston, 2016)).....	37

## LIST OF TABLES

---

<b>Table 1.</b> List of satellite data used .....	12
<b>Table 2.</b> Validation of the satellite-derived shorelines (SDS) from different satellite missions relative to the high and low waterline .....	23
<b>Table 3.</b> Mann-Kendall test in detecting monotonic trends in shoreline retreat .....	25
<b>Table 4.</b> Mann-Kendall test in detecting monotonic trends in sea-level time series .....	30
<b>Table 5.</b> Annual shoreline displacement and sea-level changes .....	31
<b>Table 6.</b> Correlation between annual shoreline displacement and annual mean sea-level .....	32
<b>Table 7.</b> Correlation between annual shoreline displacement and annual maximum sea-level .....	33

## ACRONYMS

---

<b>ESA</b>	: European Space Agency
<b>MIR</b>	: Mid-infrared
<b>NIR</b>	: Near-infrared
<b>SWIR</b>	: Short-wavelength Infrared
<b>R</b>	: Red band
<b>G</b>	: Green band
<b>B</b>	: Blue band
<b>SDS</b>	: Satellite-derived shoreline
<b>USGS</b>	: United States Geological Survey
<b>GIS</b>	: Geographic Information System
<b>DSAS</b>	: Digital Shoreline Analysis System
<b>NSM</b>	: Net Shoreline Movement
<b>EPR</b>	: End Point Rate
<b>LRR</b>	: Linear Regression Rate
<b>MAPE</b>	: Mean Absolute Percentage Error
<b>MNDWI</b>	: Modified Normalized Difference Water Index
<b>NDWI</b>	: Normalized Difference Water Index
<b>DTM</b>	: Digital Terrain Model
<b>GMSL</b>	: Global Mean Sea Level
<b>GEE</b>	: Google Earth Engine
<b>SAR</b>	: Synthetic Aperture Radar
<b>MSI</b>	: Multi-Spectral Instrument
<b>ETM+</b>	: Enhanced Thematic Mapper Plus
<b>OLI</b>	: Operational Land Imager
<b>SLR</b>	: Sea-level rise
<b>IPCC</b>	: Intergovernmental Panel on Climate Change
<b>RMSE</b>	: Root Mean Square Error

# 1. INTRODUCTION

## 1.1. Background

More than 50 % of the global population dwell within 100 km of the coast (Toure, Diop, Kpalma, & Maiga, 2019). The coastal zones in Senegal form a significant economic asset for the country (Bakhoum et al., 2017). However, coastal erosion and flooding have caused havoc to humans and destroyed many properties around the coast of Senegal, particularly in the capital, Dakar (Sane & Yamagishi, 2004). The rate of sea-level rise (SLR) due to global warming associated with subsidence has increased the risk of coastal erosion and flooding (Church & White, 2011). In the long-term, sea-level rise induces shoreline retreat (Bird, 1996; Stive et al., 2002; Pradhan, Rizeei, & Abdulle, 2018; Su & Gibeaut, 2017).

A shoreline (or coastline) is a boundary between water and land (or sand) observed at a particular time (Vos, Splinter, Harley, Simmons, & Turner, 2019). Shoreline indicators, e.g., high water line and low water line, are measurements that define a shoreline (Leatherman, 2003). The dynamic nature of the shoreline makes establishing these indicators difficult (Boak & Turner, 2005). Shoreline indicators can either be mathematical or physical. Local tide data are sources of mathematical shoreline indicators. Morphological and non-morphological indicators make up the physical indicators (Pajak & Leatherman, 2002). Shoreline monitoring is necessary to identify vulnerable coastal erosion and flooding areas, for beach monitoring, and sustainable management of the coastal environment (Toure et al., 2019; Ericson, Vörösmarty, Dingman, Ward, & Meybeck, 2006).

Detecting shorelines using surveying methods is stressful and expensive (Rumson, Hallett, & Brewer, 2017; Mirsane, Maghsoudi, Emadi, & Mostafavi, 2018). Visual inspection of high-resolution aerial images, on the other hand, needs a lot of time and a trained eye (Mirsane et al., 2018). Numerous free satellite images are available for shoreline extraction (Demir, Oy, Erdem, Seker, & Bayram, 2017). They offer possibilities for regional monitoring and analysis of coastal dynamics in a fast, efficient, and relatively cheap way (Mirsane et al., 2018).

## 1.2. Research problem

Shoreline extraction is a challenge in satellite remote sensing due to its vulnerability to dynamic processes (like sediment transport and global warming effects such as sea-level rise), as reported in various publications (e.g., Paravolidakis, Ragia, & Moirogiorgou, 2018; Nandi, Ghosh, Kundu, Dutta, & Baksi, 2016; Aedla, Dwarakish, & Reddy, 2015; ChenthamilSelvan, Kankara, & Rajan, 2014; Mukhopadhyay et al., 2012; El-Deen Taha & Elbeih, 2010; Fenster, Dolan, & Morton, 2001). For example, the main challenge of using optical sensors is that they depend on sunlight, and the images might not be usable due to the presence of clouds (Buono, Nunziata, Mascolo, & Migliaccio, 2014). However, it is easy to extract the shoreline from optical images because the spectral signatures allow discrimination of land and water

using simple approaches, possible with pixel-level accuracy (Mirsane et al., 2018). Synthetic Aperture Radar (SAR), on the other hand, is an imaging technology that operates day and night. The SAR images are not affected by weather conditions, but they are more difficult to process than optical images because they usually need terrain correction and contain speckles and noise (Demir et al., 2017). For these reasons, it will be useful to compare the results of different techniques of extracting shorelines from remotely sensed satellite (optical and SAR imaging technologies) imageries.

### **1.3. Research justification**

Evaluating the long-term shoreline evolution relative to sea-level changes will help provide insight into the dynamics and the coast's future. This study will help the stakeholders in efficient beach monitoring, erosion-accretion studies, environmental protection, and sustainable management of the coast.

### **1.4. Research objectives**

The main objective of this research is to evaluate the rate of shoreline change in Dakar (Senegal) for the last 20 years using satellite data.

The specific objectives are:

- To assess techniques for extracting shoreline from Sentinel-1 (SAR), Sentinel-2 (MSI), Landsat-7 (ETM+), and Landsat-8 (OLI) data.
- To evaluate the evolution of the shoreline from 2000 to 2020.
- To investigate the trend of sea-level rise in the area.

### **1.5. Research questions**

- How similar are the results of the shoreline extraction techniques?
- What is the magnitude and direction of the shoreline change?
- Is the shoreline changing relative to sea-level rise?

### **1.6. Study area**

Senegal is a West African country located between latitudes 12°N and 17°N and longitudes 11°W and 18°W. The coastal area (facing the Atlantic Ocean) is made up of long sandy coastline stretches, the Senegal Delta, a small stretch of rocky shoreline, and the sheltered shorelines (of the Saloum and Casamance). The open and sheltered coasts have a total length of about 500 km and 1565 km, respectively (Clemens et al., 1995). The study area is in Dakar (the capital and the largest city in Senegal), located in the western part of Senegal (Figure 1). The region considered is a sandy shoreline that stretches across Malika and Gadaye beaches. Sandy shorelines are prone to abrupt changes due to environmental conditions (Wright & Short, 1984). According to Sagne et al. (2020), the beaches at Malika and Gadaye are faced with severe erosion, attributed to their low topography and absence of barriers against swells.

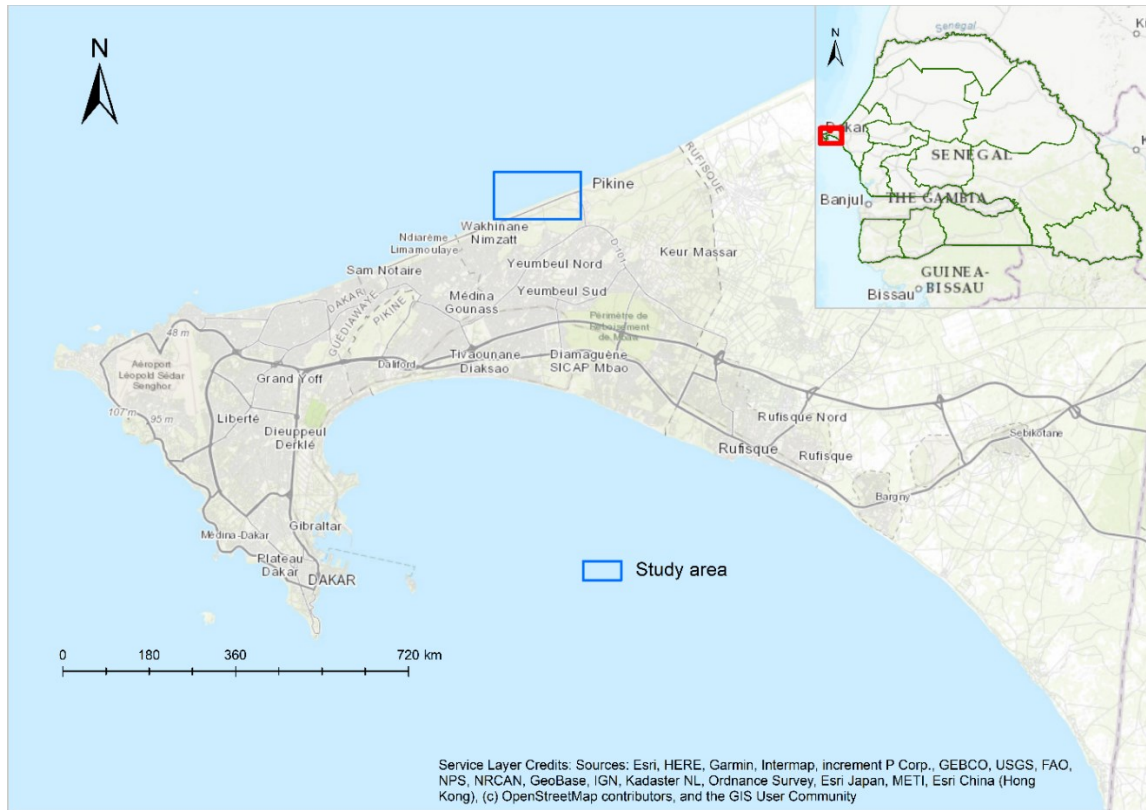


Figure 1. Study area in Senegal.

## 2. CONCEPTUAL FRAMEWORK AND RELATED WORKS

This chapter explains some basic concepts and literature (background) related to shoreline detection, most importantly getting information from those associated with the study area. This background focuses on information about shoreline indicators, sea-level rise, and the coastal zone in Senegal. This review also covers remote sensing and GIS applications in shoreline monitoring and related studies conducted around the study area.

### 2.1. Shoreline dynamics and evolution

Episodic, short, and long term changes in sea level significantly govern shoreline movement, and a good insight into these dynamics supports the prediction of the rate of change (Grases, Gracia, García-León, Lin-Ye, & Sierra, 2020; Ryabchuk, Spiridonov, Zhamoida, Nesterova, & Sergeev, 2012). Various other physical factors also influence shoreline changes, namely wind, waves, currents, the supply of sand (Thoai, Dang, & Kim Oanh, 2019), and human activities (Hauser et al., 2017). The rate of sand supply affects how the shoreline evolves at a particular location (Stronkhorst, Huisman, Giardino, Santinelli, & Santos, 2018). The coastal environment can vary from open coasts to coastal areas sheltered from waves or next to a seawall, adjacent to a tidal channel, etc. (Amaroli, Ciavola, Balouin, & Gatti, 2006).

Episodic changes happen due to abrupt tectonic movements, tropical storms, or hurricanes (Grases et al., 2020). Short-term changes occur over a few tens of years and vary along the coastline. Long-term changes occur in tens to thousands of years. Determination of average annual rates incorporates estimation of these changes (Ryabchuk et al., 2012).

### 2.2. Identification of shoreline indicators

Berm crest, vegetation, scarp edges, and dunes are regarded as morphological indicators. Non-morphological (sand wetness and waterline) can be identified from satellite images (Pajak & Leatherman, 2002). The non-morphological indicators are identified as the previous high water (backshore) line (PHWL), the high water line (HWL), instantaneous water line (IWL), and low water (tidal plain) line (LWL). These lines are dynamic, and the positions are influenced by the sea state (van der Werff, 2019). Figure 2 presents a sketch of the commonly used shoreline indicators.

Boak & Turner (2005) carried out a review of the definition and detection of shoreline. They reported that the data sources for identifying shoreline indicators are historical land-based photographs, coastal maps, and charts, aerial photography, beach surveys, GPS shorelines, Remote sensing (multispectral/hyperspectral) imaging, airborne light detection, and ranging technology (LIDAR), microwave sensors, and video sensors).

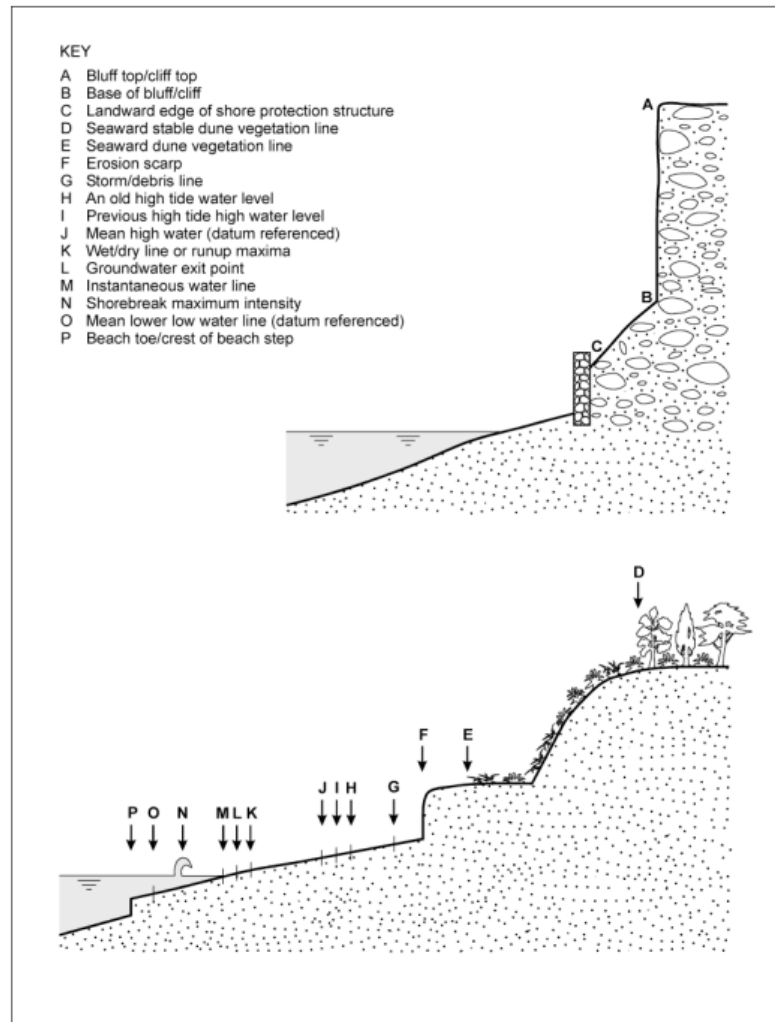


Figure 2. Schematic representation of the spatial relationship between typical shoreline indicators (Source: Boak & Turner (2005)).

### 2.3. Remote sensing application in shoreline extraction

Shoreline monitoring using remote sensing has become widely embraced by coastal engineers, coastal scientists, and coastal managers. Shorelines may be derived based on visual interpretation of coastal features, a specified tidal datum, or digital image-processing analysis (Boak & Turner, 2005).

#### 2.3.1. Optical satellite imagery

Since the launch of the Landsat satellite in 1972, medium-resolution optical imagery became widely accessible. Commercial high-resolution optical satellites such as IKONOS and Quickbird became available a few decades after as alternatives to airborne systems (Gens, 2010).

The advantage of optical imagery is that large areas can be covered with detailed spectral information. Shorelines can therefore be derived from the visual definition of coastal features or digital image processing techniques because the spectral information enables a better distinction and classification of land and water (Boak & Turner, 2005). However, the drawbacks of optical systems are their reliance on sunlight, and the images might not be usable when affected by clouds (Mirsane et al., 2018). Sentinel-2

images offer a higher spatial and temporal resolution than other optical images (e.g., Landsat-5, Landsat-7, and Landsat-8) that are useful for shoreline extraction (Vos et al., 2019).

### **2.3.2. Synthetic Aperture Radar (SAR) imagery**

Synthetic Aperture Radar (SAR) is an active imaging technology that uses microwaves. It penetrates through clouds, and its operation is independent of the Sun's illumination (Bamler, 2000). SAR imagery became available for shoreline extraction after the launch of the Seasat satellite in 1978 (Gens, 2010). J. Lee & Jurkevich (1990) extracted the shoreline from Seasat SAR and Shuttle Imaging Radar B (SIR-B) images by integrating an edge detection method and an edge tracing algorithm to identify a continuous shoreline. They reported that the success of the algorithm was dependent on the contrast between land and water areas and also that the SAR signal echo from the sea surface greatly depends on the sea state at the time of image acquisition. They further pointed out that for improved accuracy of the method, additional processing would be required.

Demir et al. (2017) applied random forest classification (in the segmentation of land and water) to RASAT (pan-sharpened) and Sentinel-1 (SAR) images in shoreline extraction. They compared the results with the manually digitized shoreline. The assessment of the accuracy was done by calculating perpendicular distances from the reference data and the shoreline extracted. The mean difference obtained was approximately a pixel.

H. Liu & Jezek (2004a) developed a method that incorporates Canny edge detection and local thresholding approaches in shoreline extraction from Radarsat SAR imagery (25 m resolution). Adaptive thresholding was used to segment the orthorectified SAR image while Canny edge detection was applied to process the segmented images into vector-based output. The average relative accuracy of coastline position obtained was within one image pixel.

Coastal areas usually have windy and cloudy weather conditions. Weather conditions do not affect SAR images which is an advantage (in monitoring coastal and cloudy areas) they have over optical images. However, processing of SAR data (due to the presence of noise and speckles and the need for terrain correction) is more challenging compared to optical data (Demir et al., 2017).

## **2.4. Water-land segmentation**

Segmentation is a process where attributes of an image are extracted based on intensity values (Gonzalez, Woods, & Hall, 2002). There are three categories of automated methods of shoreline extraction from satellite imagery (Zhang, Yang, Hu, & Su, 2013):

Classification methods (e.g., Modified Normalized Difference Water Index (MNDWI) (Xu, 2006), Spectral Angle Mapper (SAM) classification techniques (Rashmi, Addamani, & Ravikiran, 2014)): This approach extracts homogenous areas (or regions) into classes. The method could be pixel-based (e.g., MNDWI) or object-oriented (e.g., SAM). Pixel-based classification deals only with the spectral details of pixels and disregards their spatial arrangement. Object-oriented classification, on the other hand, deals

with the spectral, textural, contextual, and spatial information of pixels in the classification process (Toure et al., 2019).

**Edge detection:** This technique deals with identifying areas of abrupt variation in grey-level, colour (or intensity), or texture of an image. The edge detection techniques are Canny Edge detection, Snakes, and Level set algorithm (Toure et al., 2019). Snakes and Level Set Algorithm have been reported to be prone to errors and time-consuming (Yu et al., 2013; Toure et al., 2018), respectively.

**Band thresholding methods:** This technique uses a histogram to generate two classes, segmented from panchromatic images. The methods are not reliable for hyperspectral (HS) and multispectral (MS) images because details of the images will be lost when the histogram operation is applied (Toure et al., 2019).

Ghosh, Kumar, and Roy (2015) used the Modified Normalized Difference Water Index (MNDWI) over Landsat images for coastline extraction and change detection in Hatiya Island (Bangladesh). The results they obtained revealed that the island experienced erosion and accretion of 6476 hectares and 9916 hectares, respectively, from 1989 to 2010. The MNDWI method was validated by comparing the output with results obtained from manually digitizing boundaries between land and water from reference data. The accuracies obtained ranged from 88% to 95%.

de Boer et al. (2019) explored publicly available (on Google Earth Engine (GEE)) composite images of Landsat 5, 7, and 8 satellite imagery between 1 January 1984 and 1 January 2018 to assess the evolution of the beaches around the seaports in Africa. The coastlines were detected using an automated satellite-derived shoreline (SDS) algorithm based on the Normalized Difference Water Index (NDWI). A total area of 44 km<sup>2</sup> (23 km<sup>2</sup> accretion and 21 km<sup>2</sup> is erosion) was evaluated as changes in the beach area.

Konko, Bagaram, Julien, Akpamou, & Kokou (2018) analysed the spatial and temporal changes of the Togolese coast (and the nearby Lake Togo and Lake Boko) from 1988 - 2018. They combined optical and radar remote sensing in their approach. They used the Normalized Difference Water Index (NDWI) in discriminating aquatic areas, terrestrial areas, and in extracting the coastline. With the Digital Shoreline Analysis System (DSAS), their results revealed that the coastline retreated at rates ranging from 1.66 to 5.25 m/year. Lake Togo was expanding at an average rate of 1.55 m/year, while Lake Boko was shrinking at an average rate of 1.25 m/year.

Paravididakis, Ragia, & Moirogiorgou (2018) developed an automated approach for extracting coastline using Canny Edge detection and optimization operations. They compared their results with ground control points and obtained an acceptable accuracy (using RMSE) equivalent to 0.85 m.

#### **2.4.1. Modified Normalized Difference Water Index (MNDWI)**

The MNDWI is a technique that reduces the signal from land (built-up areas) so that extracted water features are not mixed up with the built-up areas (Xu, 2006). The near-infrared (NIR) band in the Normalized Difference Water Index (NDWI) (McFeeters, 1996) (see equation (1)) is substituted with the mid-infrared (MIR) band in the MNDWI. Mathematically, the MNDWI can be calculated (as shown in

equation (2)) by subtracting the values of mid-infrared (MIR) reflectance from green (Green) reflectance (Figure 3) and dividing it by the sum of both.

$$NDWI = \frac{Green - NIR}{Green + NIR} \quad (1)$$

$$MNDWI = \frac{Green - MIR}{Green + MIR} \quad (2)$$

The values of MNDWI range from -1 to +1. Water will have positive values (greater than in the NDWI) as it has a lower reflectance in the MIR band than in the Green band, whereas land and built-up areas will have negative values since they have higher reflectance in the MIR than in the Green band. A binary approach will be applied over the MNDWI images to obtain land and water classes. Subsequently, the classified image will be converted to vector format.

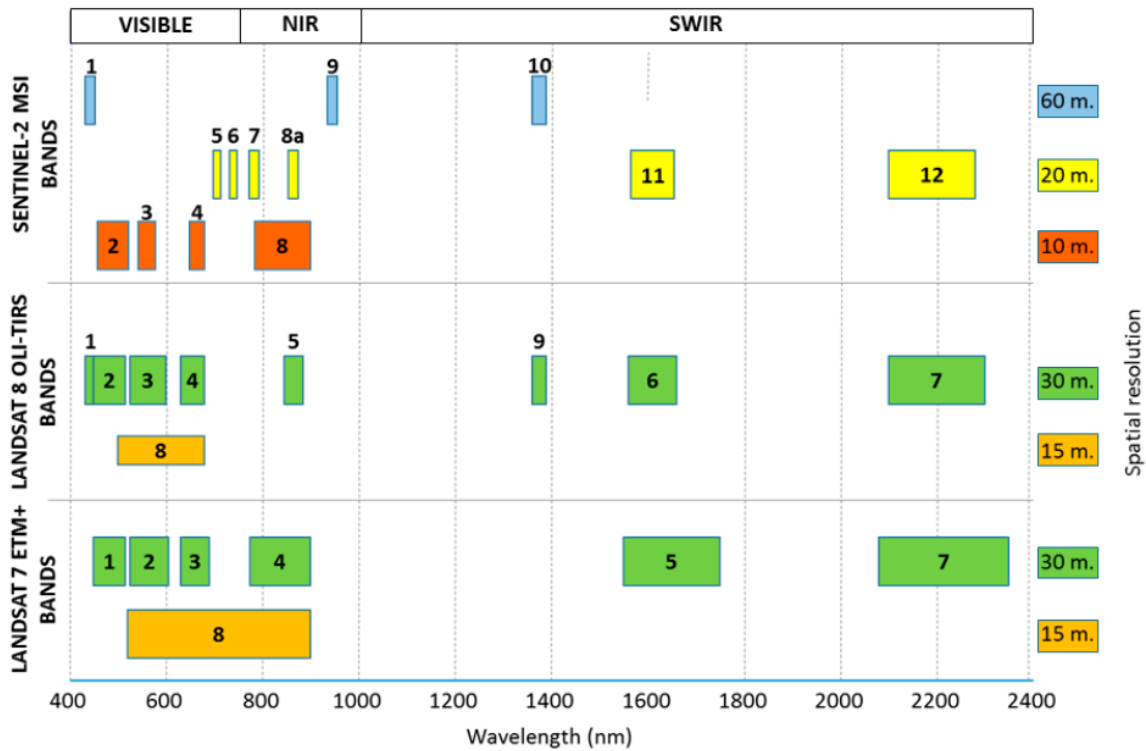


Figure 3. Spatial resolution and spectral range of Landsat (7 and 8) and Sentinel-2 bands (in the optical spectral region) (Source: (Pardo-Pascual et al., 2018)).

#### 2.4.2. Adaptive thresholding

This method is based on partitional clustering (K-means) (Macqueen, 1967; Anderberg, 1973; Fu & Mui, 1981) that considers only two (e.g., land and sea) clusters to produce a binary image. Clustering is a process of segmenting an image such that elements with similar reflectance are grouped in the same cluster (Bhatia, 2004). K-means clustering considers that each element in the image has a location in space. It further creates partitions (using an iterative process) such that elements within each class (or cluster) are close to each other (based on their mean and standard deviation) and far enough from elements in other clusters (Paravolidakis et al., 2018). The threshold clustering algorithm assigns two elements to be in the

same cluster if the distance separating them is below an assigned threshold. Details of the steps of the algorithm (Bhatia, 2004) are as follows:

- An element is selected and assigned the seed of a particular cluster
- The distance of an unclassified element is compared with the mean (or centroid) of existing clusters. It will be assigned to a cluster if the distance is less than the specified threshold. Otherwise, the element is passed to a new cluster.
- The iteration stops after all elements have been placed in matching clusters.

### 2.4.3. Canny Edge Detection

Canny Edge detection (Canny, 1986) is a technique that detects the edge pixels in an image. The details of the algorithm can be simplified in the following steps (H. Liu & Jezek, 2004; Zheng, Lei, Yao, Gong, & Yin, 2018):

#### Gaussian filter

In Canny Edge detection, a Gaussian filter is applied to smoothen (blur) the image. The main purpose of applying the filter is to remove noise.

#### Calculation of gradient value and direction

The Canny Edge detection algorithm applies four operators to detect edges (in the blurred image) in the horizontal, vertical, and diagonal directions. The technique uses the Sobel operator to obtain the values of the first derivative in the horizontal ( $G_x$ ) and vertical directions ( $G_y$ ) in order to calculate the gradient ( $G$ ) (equation (3)) and direction ( $\theta$ ) of the pixel points (equation (4)).

$$G = \sqrt{G_x^2 + G_y^2} \quad (3)$$

$$\theta = \arctan \frac{G_y}{G_x} \quad (4)$$

#### Non-maximum suppression

This process helps to identify areas with local maximum gradient values (change of intensity) and leaving out lower values. This operation recognises the gradient intensity of the current pixel as an edge point only if it is larger than the gradient intensities of the pixels in the positive and negative gradient directions otherwise, it will be suppressed. For better accuracy, linear interpolation is applied between the adjacent pixels to obtain the gradient direction of the current pixel.

#### Double threshold detection

The algorithm applies double (high and low) threshold values in detecting the edge pixels. Edge pixel gradients larger than the high threshold are detected as strong edge points. An edge gradient lower than the high threshold but larger than the low threshold is identified as a weak edge point. The edge pixel gradients are suppressed if they are lower than the low threshold.

### Boundary (Edge) tracking by hysteresis

The edge boundary tracking by hysteresis is done to ascertain that only strong edge pixels are retained in the final image. A weak edge that is connected to a true edge will be linked to a strong edge pixel. The algorithm trails the 8-connected surrounding pixels of a weak edge pixel to preserve strong edge pixels and discard non-edge pixels.

## **2.5. Literature review**

Toure et al. (2019) reviewed shoreline detection approaches using optical remote sensing. They reported that the methods adopted relied on the resolution of the image and the proposed application. Toure, Diop, Kpalma, and Maiga (2018) applied image segmentation clustering to separate different classes (waves, dry sand, wet sand, and land) and edge detection to an image from Google Earth in detecting the shoreline. Distance Regularization Level Set Evolution (DRLSE) was applied to set the limit for the average level of high water tide and improve the accuracy of the extracted shoreline. They found that the technique was effective because the results obtained were very similar to ground truth data with a Root Mean Square Error (RMSE) of 0.2 m.

Bakhomou et al. (2017) extracted shoreline positions of Goree Island (Senegal) from an aerial photograph (1942, 1966, and 2011) using ArcGIS software and the Digital Shoreline Analysis System (DSAS). They also applied End Point Rate (EPR) and Net Shoreline Movement (NMS) in estimating the rate of change. The results they obtained revealed that the shoreline retreated at a mean rate of -0.16 m/year and -0.06m/year between 1942 to 1966 and 1966 and 2011, respectively.

Thior et al. (2019) studied the dynamics of the coastline linking northern Casamance (Senegal) and southern Gambia using multi-date images (1968 aerial photographs captured by France National Geographic Institute (IGN), 1986 Landsat images, and Google Earth images of the years 2004 and 2017). After identifying a coastal reference line and image correction, they digitized the coastline, then applied the DSAS to estimate uncertainty and calculate the rate of change of the coastline. They found out that the study area experienced accretion between 1968 and 1986 and erosion between 1986 and 2004.

Pardo-Pascual et al. (2018) evaluated the accuracy of the positions of shorelines extracted from the infrared bands of satellite images (Landsat 7, Landsat 8, and Sentinel-2) on beaches. Reference lines of the respective images (taken at the expected scene registration time) were used to assess the errors. Each shoreline (sub-pixel) was connected by points. The distances between the points and the reference line revealed the error (positive (seaward) and negative (landward)). The mean error was an indication of the satellite-derived shoreline bias. On the other hand, the standard deviation revealed the difference in shoreline position at the instance of image registration.

Cozannet et al. (2015) used satellite synthetic aperture radar interferometry to characterise vertical coastal ground motion velocities in Dakar (Senegal) from 1992–2010. They found out the differential ground motion in Dakar was low (not exceeding 1mm year<sup>-1</sup>). However, the ground motions had no effect on the historical tide gauge (sea-level) records of Dakar.

### 3. RESEARCH METHODOLOGY

#### 3.1. Work Flow

This chapter describes the methodology followed (Figure 4) to achieve the desired objectives and answer the research questions. This research intends to evaluate the rate of shoreline changes in Dakar (Senegal) for the last 20 years using satellite data.

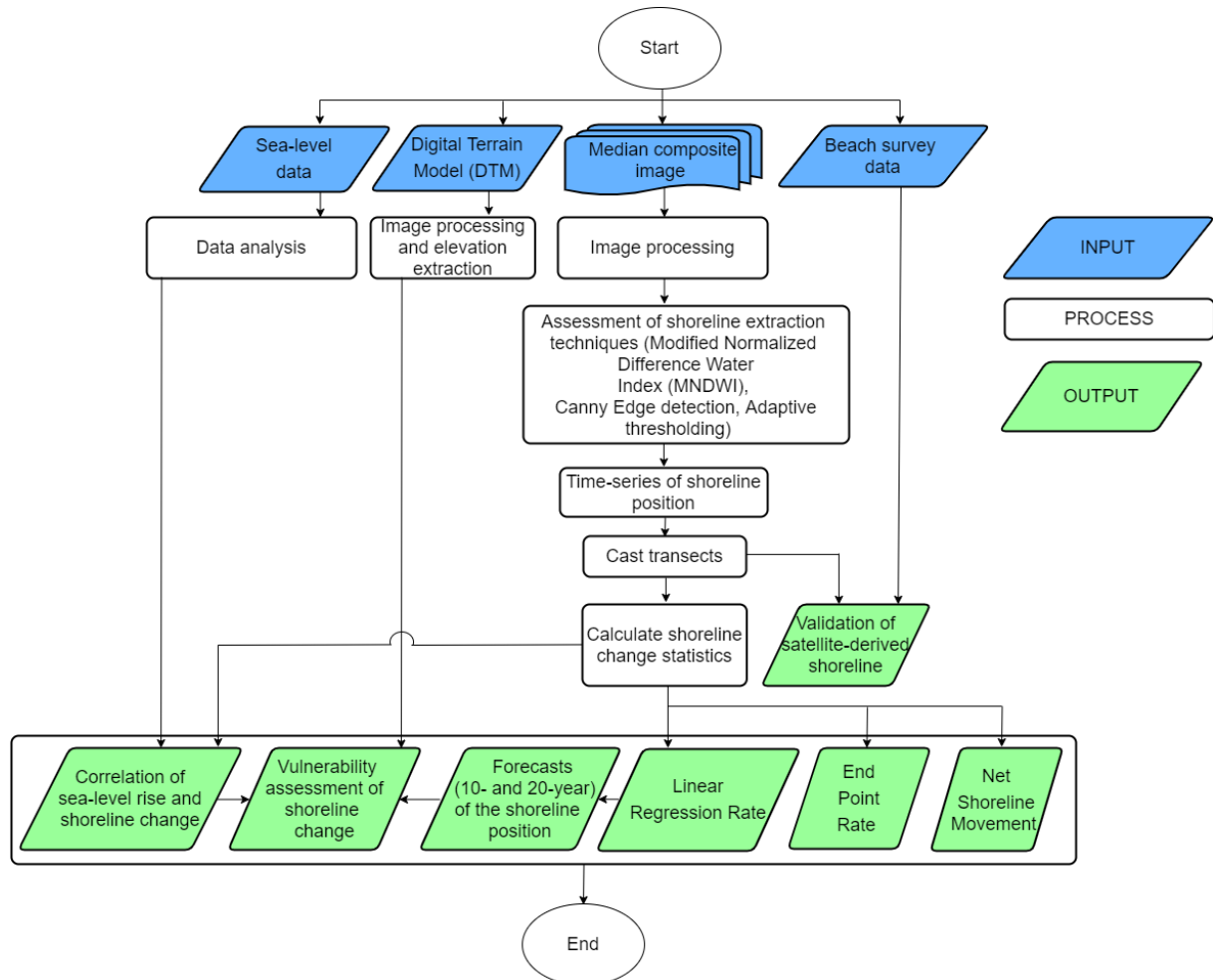


Figure 4. Flowchart of the methodology for the study.

#### 3.2. Data collection

##### 3.2.1. Field data

A beach survey of the high and low waterline was done with a differential GPS by the Ecological Monitoring Centre in Senegal on 16 December 2020. Series of points were recorded every 50 meters along the high and low waterline. The sea-level data was retrieved from the University of Hawaii Sea Level Center website (<http://uhscl.soest.hawaii.edu/data/>).

### 3.2.2. Satellite data

Annual median (median pixel value) composites of optical and Synthetic Aperture Radar (SAR) images were used in this study to minimise the effect of clouds (particularly in optical images) and tides (Dimosthenis Traganos, Poursanidis, Aggarwal, Chrysoulakis, & Reinartz, 2018). Median composite Landsat-7 (Enhanced Thematic Mapper Plus (ETM+)), Landsat-8 (Operational Land Imager (OLI)), and Sentinel-2 (Multispectral Instrument (MSI)) images were obtained from the Google Earth Engine (GEE) platform (<https://code.earthengine.google.com>). Sentinel-1 (SAR) images were obtained from the Alaska Satellite Facility Data Search website (<https://search.asf.alaska.edu/#/>). Digital Elevation Model (Shuttle Radar Topography Mission (SRTM)) was obtained from the United States Geological Survey Earth Explorer website (<https://earthexplorer.usgs.gov/>). The detailed information about the satellite data can be seen in Table 1.

Table 1. List of satellite data used

Mission	Instrument	Image resolution	Date
Sentinel-1	SAR	10 m	2016 - 2020
Sentinel-2	MSI	10 m R, G, B, NIR; 20 m SWIR1	2016 - 2020
Landsat-7	ETM+	30 m R, G, B, NIR, SWIR1 bands; 15 m panchromatic band	2000 - 2012
Landsat-8	OLI	30 m R, G, B, NIR, SWIR1 bands; 15 m panchromatic band	2013 - 2015
SRTM	SAR	30 m	2000

### 3.3. Satellite image processing

#### 3.3.1. Synthetic Aperture Radar (Sentinel-1) image processing

The SAR data used in this study is Sentinel-1 level 1 Ground Range Detected (GRD) images (available from 2016 – 2020) with Interferometric Wide Swath (IW). The individual images were mosaicked and processed by applying the common workflow (Filipponi, 2019) within ESA's Sentinel Application Platform (SNAP). The steps involved are: Apply orbit file, thermal noise removal, calibration, terrain correction, speckle filtering, linear to decibel (dB) conversion, and reprojection.

The GRD (Sentinel-1 level 1) products have been multi-looked and projected (to the ground range). Apply orbit file operation is done to update the orbit details of the SAR scenes. Thermal noise removal minimises the noise effects (incoherence), resulting in multi-swath acquisition scenes. Calibration transforms the values of the pixels (image intensity) to sigma nought (calibrated SAR backscatter) values. Terrain (range doppler) correction was done (using 30 m SRTM) to rectify the geometric distortion (of each pixel) caused by topography (foreshortening and shadows). The image quality was improved during speckle filtering (using the refined Lee filter (J. S. Lee, Jurkevich, Dewaele, Wambacq, & Oosterlinck,

1994)) to preserve texture information and edges. The backscatter coefficient (unitless) was converted to decibel (dB). The final output was reprojected (EPSG 32628: WGS 1984 – UTM Zone 28 N) to the coordinate reference system of the study area (Filipponi, 2019).

### **3.3.2. Optical image processing**

Cloud masking: The Quality Assessment band of each image contains a per-pixel cloud mask. This information is generated by the data provider (ESA for Sentinel-2 or USGS for Landsat) based on the number of cloudy pixels in a region of interest (Vos et al., 2019). The search was limited to images with less than 40% cloud cover, and subsequently, median composite images were obtained to further minimise the effect of tides and cloud shadow (Dimosthenis Traganos et al., 2018). Top-of-Atmosphere (TOA) reflectance Landsat images were used in this study because it presents a representative comparison between images (Chander, Markham, & Helder, 2009). Co-registration and processing of Landsat images were done on the GEE platform before downloading. Co-registration was carried out because the misregistration (or misalignment) between Landsat and Sentinel images can go beyond 38 m (Storey et al., 2016).

The panchromatic band (15 m) of Landsat-7 and Landsat-8 was used to down-sample the multispectral bands from 30 m to 15 m (by bilinear interpolation). This was done by replacing the first principal component (principal component analysis) with the panchromatic band (Tu, Su, Shyu, & Huang, 2001). Sentinel-2 level 1C images were used in this study. The mid-infrared (SWIR1) band was down-sampled to 10 m (by bilinear interpolation) for a uniform resolution (10 m) for all bands (Vos et al., 2019).

### **3.3.3. Digital Terrain Model (DTM) processing and elevation extraction**

The DTM was reprojected (using ArcGIS 10.7.1) to the coordinate reference system of the study area (EPSG 32628: WGS 1984 – UTM Zone 28 N). The reprojected DTM was then reclassified to extract the elevation of the area.

## **3.4. Shoreline extraction**

### **3.4.1. MNDWI technique**

MNDWI (Xu, 2006) was applied to the optical images (using the Green and Mid-infrared (MIR) bands) to classify the pixels into two (land and water) classes using ArcGIS 10.7.1 software. The jagged edges of the shorelines were smoothed using a low pass filter (3x3) (Dewangan & Kumar Sharma, 2017). The MNDWI image was converted to polygon (vector file) then to line features (using the polygon to line tool in ArcGIS 10.7.1) afterward. Finally, the delineated shoreline was extracted.

### **3.4.2. Canny Edge Detection Algorithm**

Canny Edge Detection (Canny, 1986; H. Liu & Jezek, 2004) was applied to SAR (Sentinel-1) and optical (MIR band of Sentinel-2) images on GEE platform to delineate the shoreline from the edge pixels at the land-sea boundary. GEE provides the inherent implementation of Canny Edge detection algorithm

identifying edges from images. The Canny Edge Detection image was exported as a raster (.tif format) then imported into ArcGIS 10.7.1 environment. The raster image was smoothed (low pass filtering) and converted to polygon. Subsequently, the polygon was converted to lines (using the polygon to line tool in ArcGIS 10.7.1) for extraction of the shoreline.

### 3.4.3. Adaptive thresholding technique

Adaptive thresholding (H. Liu & Jezek, 2004; Aedla, Dwarakish, & Reddy, 2015) was applied to the optical images (using the Mid-infrared (MIR) band) to group the pixels into two (land and water) clusters using ArcGIS 10.7.1 software. The segmented image was smoothed (low pass filtering), converted to polygon (vector file), and subsequently to lines. The shoreline was finally extracted from the line features.

### 3.5. Shoreline validation

The beach survey points (of the high and low waterline) acquired using a GPS were converted to line features in the ArcGIS v10.7.1 environment. The validation was carried out on shorelines extracted from Landsat-7, Landsat-8, and Sentinel-2 median composite images. The median composites were obtained from images available within the two (2) weeks date range window (01 December 2020 – 31 December 2020) centred around the beach survey date.

The Digital Shoreline Analysis System (DSAS) (Himmelstoss, Henderson, Kratzmann, & Farris, 2018) was used in validating the shorelines. DSAS is an extension (created by United States Geological Survey (USGS)) within Esri's Geographic Information System (ArcGIS) software that can create a baseline, cast transects, and calculate rate-of-change statistics of shoreline (vector) time series data. The high and low waterline were selected as baselines in separate validations of the shorelines. Transects were cast from respective baselines and clipped to the shorelines at 50 m intervals with a search distance of 170 m (National Oceanography Centre, 2020). The offset (residual) of the shorelines from baseline was obtained from the distance between the intersection points of each transect. Offset values are either zero, positive, or negative, signifying a seaward (towards the sea) or a landward (towards the land) shift. Root Mean Square Error (RMSE) was used in assessing the accuracy (validation) of the satellite-derived shorelines (SDS). The RMSE (equation (5)) was obtained as follows:

$$\text{RMSE} = \sqrt{\left[ \frac{(\text{residuals})^2}{\text{number of transects intersected}} \right]} \quad (5)$$

### 3.6. Shoreline evolution

The shoreline change from 2000 to 2020 was calculated with the DSAS. The process involves four main steps (Himmelstoss et al., 2018): baseline creation, casting transects, calculating statistics, and forecasting. The baseline was created by selecting the earliest year (2000) shoreline. Transects were cast from the baseline to clip the shorelines at 50 m intervals (with a search distance of 170 m). The Net Shoreline Movement (NSM) and End Point Rate (EPR) were determined to calculate the shoreline change rates. The Net Shoreline Movement (NSM) is obtained as the distance between the oldest and the most recent

shoreline for respective transects. The EPR, on the other hand, is the ratio between the NSM (in meters) and the period (in years) between the oldest and the most recent shoreline position. The linear regression rate-of-change (LRR) statistic for a transect can be derived from the fitted least-squares regression line to all shoreline points. The slope of the line gives the LRR. The DSAS uses the linear regression rate in calculating (forecasting) the future positions of the shoreline for the next 10 and 20 years with uncertainty regions of 10m (that lie within 95% confidence level). This process uses a Kalman filter (Kalman, 1960) in combining observed shoreline positions with positions derived from the model (DSAS).

### 3.7. Vulnerability assessment of shoreline change

The predicted positions (10- and 20-year forecasts) of the shoreline were overlaid on the elevation map (generated from the DTM) of the area to discriminate elevated areas from low-lying areas and identify locations that are vulnerable to the future (predicted) positions of shoreline.

### 3.8. Shoreline and sea-level data analysis

The parameter used in the statistical analyses are: the intercept and slope of the regression line, Pearson's correlation coefficient ( $r$ ), coefficient of determination ( $R^2$ ), the Mean Absolute Percentage Error (MAPE). The slope and intercept are the steepness of the regression line and the point of intersection of the regression line with the y-axis, respectively (Hoffmann, 2010). Practically, the slope depicts the rate of change of a variable due to the effect of another variable. Similarly, the intercept represents the increase of a variable due to the effect of another variable (Siswati, Mahanal, Susilo, & Corebima, 2016).

The Pearson's correlation coefficient ( $r$ ) assesses the linear relationship of two variables. The value (unitless) of the correlation coefficient has a magnitude in a positive or negative direction that ranges from  $-1$  to  $0$  to  $+1$ . A coefficient of zero signifies no association between the variables, but a more linear association is established between the two variables as the coefficient approaches  $-1$  or  $+1$ . A positive coefficient implies that the second variable (the criterion) increases in response to an increase in the first variable (the predictor). In contrast, a negative correlation coefficient implies that the second variable decreases in response to a rise in the first variable (Taylor, 1990). The formula (Zhou, Deng, Xia, & Fu, 2016) for calculating Pearson's correlation coefficient is presented in equation (6).

$$r_{xy} = \frac{\sum_{i=1}^n (x_i - \bar{x})(y_i - \bar{y})}{\sqrt{[\sum_{i=1}^n (x_i - \bar{x})^2][\sum_{i=1}^n (y_i - \bar{y})^2]}} \quad (6)$$

where  $n$  is the sample size,  $\bar{x}$  is the mean of  $x$  ( $\bar{x} = \frac{1}{n} \sum_{i=1}^n x_i$ ),  $\bar{y}$  is the mean of  $y$  ( $\bar{y} = \frac{1}{n} \sum_{i=1}^n y_i$ ).

The coefficient of determination ( $R^2$ ) is used in assessing the goodness of fit in a linear regression model.  $R^2$  corresponds to the square of the multiple correlation coefficient (Cheng, Shalabh, & Garg, 2014).

The MAPE assesses the quality of regression models. It interprets the model in terms of the relative error (de Myttenaere, Golden, Le Grand, & Rossi, 2016). It is the mean of absolute percentage errors

(equation (7)) (Kim & Kim, 2016). MAPE has been widely used and found to be appropriate in forecasting applications (Armstrong & Collopy, 1992).

$$\text{MAPE} = \frac{1}{N} \sum_{t=1}^N \left| \frac{A_t - F_t}{A_t} \right| \quad (7)$$

where  $N$  denotes the number of data points,  $A_t$  and  $F_t$  are actual and forecast values (at data point  $t$ ).

The P-value and the Mann-Kendall test were used to test the significance of the statistical analyses. The P-value is the probability that the selected test statistic would not have been larger than its observed value if the assumption of the model were correct (including the test hypothesis) (Greenland et al., 2016). The Mann-Kendall test (Mann, 1945; Kendall, 1975) is a non-parametric test that considers the relation between the order and sequences of a time series. The assumption of the null hypothesis  $H_0$  of a given time series  $\{x_i, i = 1, 2, \dots, n\}$  is that it is independently distributed, whereas the alternative hypothesis  $H_1$  assumes that a monotonic trend exists (Wang et al., 2020). The test statistic (S) (Mann, 1945; Kendall, 1975) is obtained using equation (8):

$$S = \sum_{i=1}^{n-1} \sum_{j=i+1}^n \text{sgn}(x_j - x_i) \quad (8)$$

where  $n$  is the number of observations (length of the time series),  $x_i$  and  $x_j$  are data values of sequence (time series)  $i$  and  $j$  ( $j > i$ ), respectively, and  $\text{sgn}(x_j - x_i)$  denotes the sign function obtained using equation (9):

$$\text{sgn}(x_j - x_i) = \begin{cases} +1, & \text{if } x_j - x_i > 0 \\ 0, & \text{if } x_j - x_i = 0 \\ -1, & \text{if } x_j - x_i < 0 \end{cases} \quad (9)$$

The variance ( $\text{Var}(S)$ ) is obtained using equation (10):

$$\text{Var}(S) = \frac{n(n-1)(2n+5) - \sum_{i=1}^m t_i(t_i-1)(2t_i+5)}{18} \quad (10)$$

where  $n$  is the length of the time series,  $m$  is the number of tied ranks, and  $t_i$  represents the number of ties (of extent  $i$ ). A group of tied ranks represents a set of sample data with the same value. If the sample size  $n > 10$ , the standard normal test statistic  $Z_S$  is obtained using equation (11):

$$Z_S = \begin{cases} \frac{S-1}{\sqrt{\text{Var}(S)}}, & \text{if } S > 0 \\ 0, & \text{if } S = 0 \\ \frac{S+1}{\sqrt{\text{Var}(S)}}, & \text{if } S < 0 \end{cases} \quad (11)$$

Positive values of  $Z_S$  signify increasing trends, while negative  $Z_S$  values indicate decreasing trends. The trends are tested at the specific significance level ( $\alpha$ ). At  $\alpha = 0.05$  (5% significance level), the null hypothesis (no trend) is rejected if  $|Z_S| > 1.96$  and rejected if  $|Z_S| > 2.576$  at  $\alpha = 0.01$  (1% significance level) (Gocic & Trajkovic, 2013). At a 5% significance level ( $\alpha = 0.05$ ), if the p-value  $\leq 0.05$ , then the trend is statistically significant. (Yue & Wang, 2004).

The Mann-Kendall test has been widely used in testing the significance of monotonic trends, especially in hydrometeorology (e.g., Douglas, Vogel, & Kroll, 2000; Yue, Pilon, & Phinney, 2003). Wahl, Jensen, Frank, & Haigh (2011) applied the Mann-Kendall in testing to assess the significant trends of sea-level time series from tide gauge data.

## 4. RESULTS AND DISCUSSION

### 4.1. Results

#### 4.1.1. Shoreline extraction and validation

The techniques applied in the extraction of the shorelines were assessed to identify a suitable approach for evaluating the evolution of the shoreline. Each methods' performance was examined by overlaying the shoreline derived over the source image. Results of shorelines extracted using adaptive thresholding techniques were compared against MNDWI-derived shorelines from 2010 Landsat-7 (Figure 5), 2013 Landsat-8 (Figure 6), and 2020 Sentinel-2 (Figure 7) median composite images. Shorelines derived using Canny Edge Detection on 2020 Sentinel-1 (Figure 8) and 2020 Sentinel-2 (Figure 9) median composite images were compared to assess their similarity.

Shorelines extracted using MNDWI delineate a clear and continuous land-sea boundary (Figure 5(a), Figure 6(a), and Figure 7(a)). The adaptive thresholding method displays limitations in identifying the line separating water and land in the Landsat-7 (2010) median composite image (Figure 5(b)).

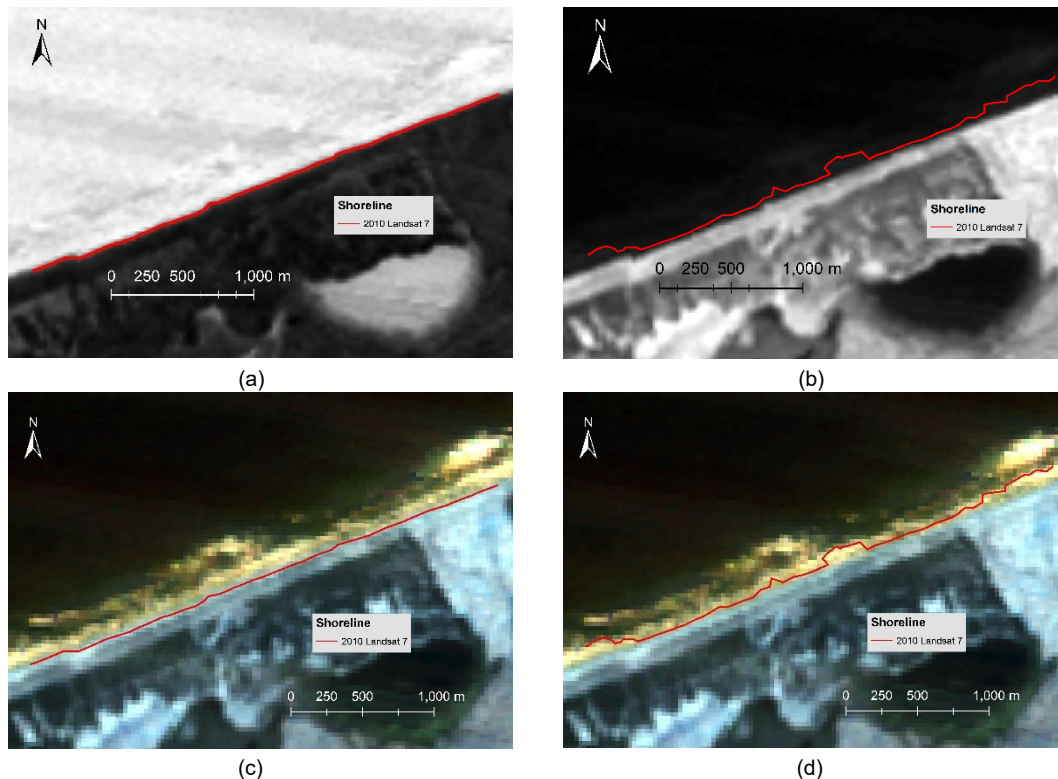


Figure 5. Overlay of shoreline extracted from 2010 Landsat-7 median composite image using (a) MNDWI (on MNDWI image), (b) adaptive thresholding (on MIR band), (c) MNDWI (on RGB composite image), (d) adaptive thresholding (RGB composite image).

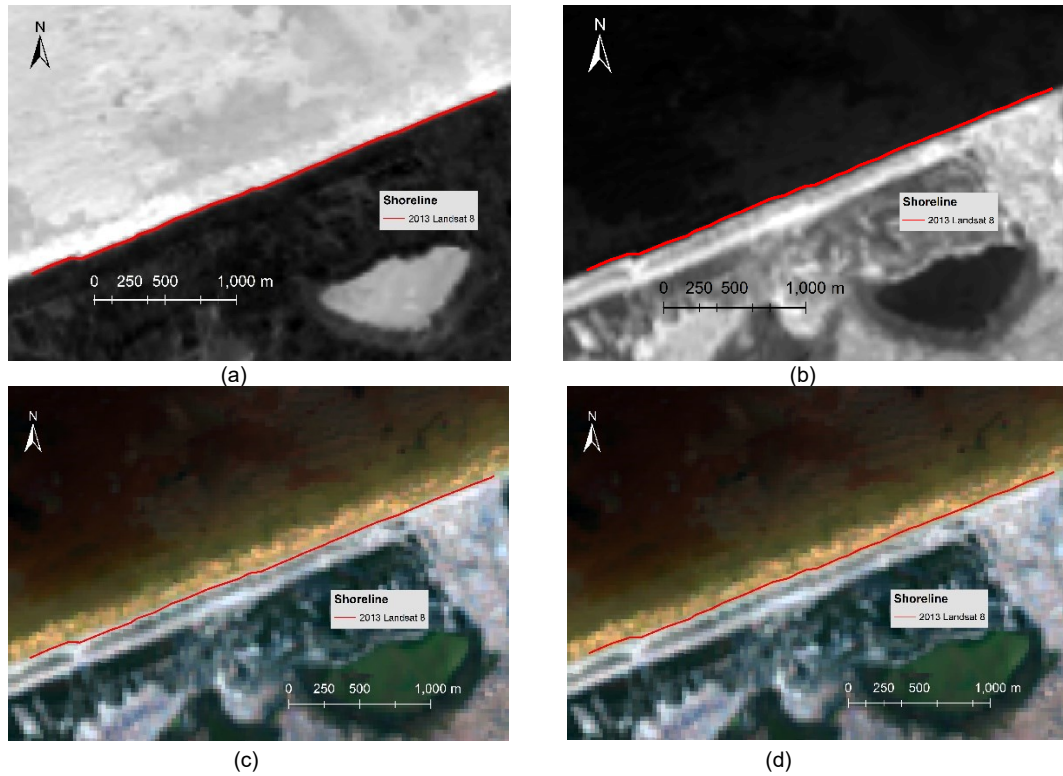


Figure 6. Overlay of shoreline extracted from 2013 Landsat-8 median composite image using (a) MNDWI (on MNDWI image), (b) adaptive thresholding (on MIR band), (c) MNDWI (on RGB composite image), (d) adaptive thresholding (RGB composite image).

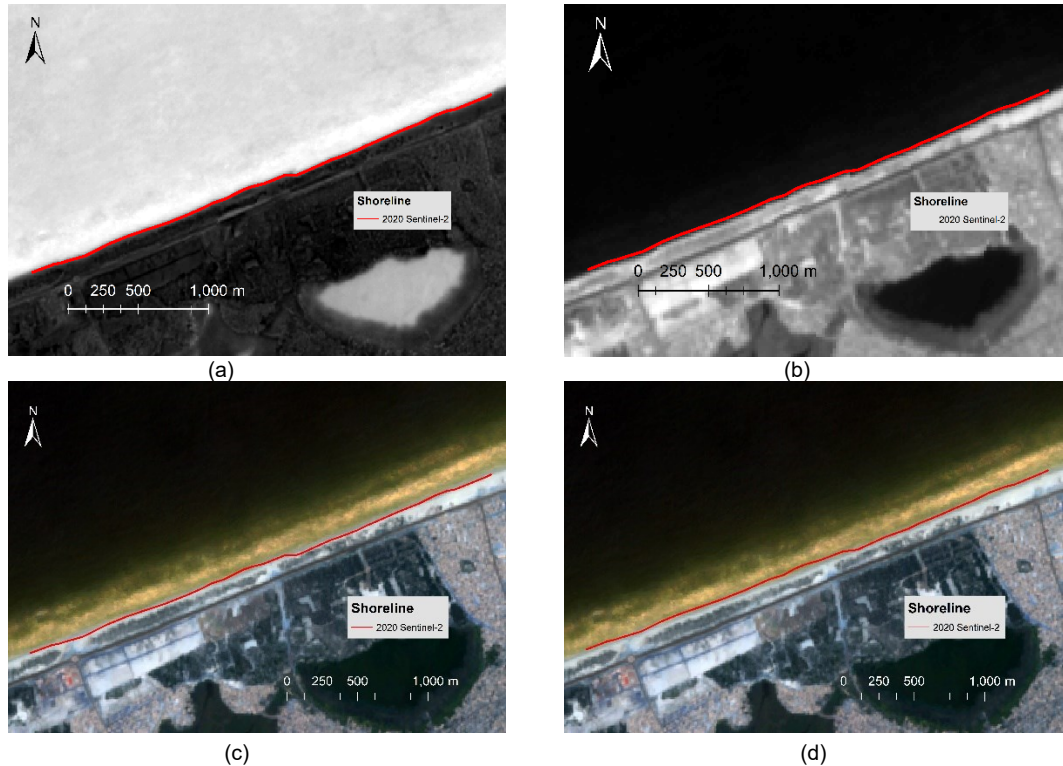


Figure 7. Overlay of shoreline extracted from 2020 Sentinel-2 median composite image using (a) MNDWI (on MNDWI image), (b) adaptive thresholding (on MIR band), (c) MNDWI (on RGB composite image), (d) adaptive thresholding (RGB composite image).

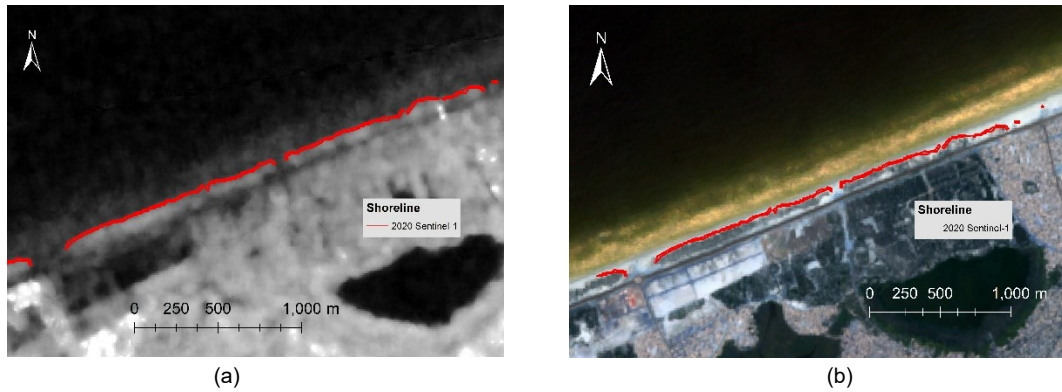


Figure 8. Overlay of shoreline extracted from 2020 Sentinel-1 median composite using Canny Edge Detection on (a) 2020 Sentinel-1 median composite image, (b) 2020 Sentinel-2 median composite, (RGB) image.

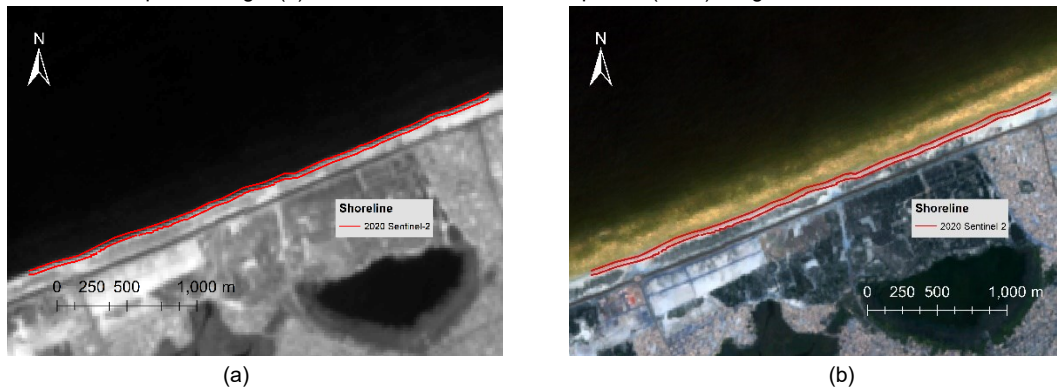


Figure 9. Overlay of shorelines extracted from 2020 Sentinel-2 median composite image using Canny Edge Detection on (a) 2020 Sentinel-2 median composite (MIR band), (b) 2020 Sentinel-2 median composite (RGB) image.

Canny Edge Detection applied on 2020 Sentinel-1 median composite image (Figure 8(a)) identifies the contrast between vegetation (Figure 8(b)) and sand as a strong edge but not the shoreline. This limitation is observed because the method identifies the abrupt change in intensity of the SAR signal between the vegetation and the beach sand during the non-maximum suppression. Another drawback of the technique is that the preservation of only strong edges created gaps (in the edges extracted) where vegetation is replaced by sand (Figure 8(b)).

Canny Edge Detection executed on 2020 Sentinel-2 median composite image delineates two edges of the shore (after cleaning up edges that are non-shorelines). The edges extracted were not continuous at areas with a non-abrupt change in intensity (Figure 9(a) and Figure 9(b)). The two edges were generated because a strong edge was identified, and weak edge pixels connected to strong edge pixels were also preserved.

Shorelines extracted using MNDWI from 2020 median composite (01 December 2020 to 31 December 2020) images of Landsat 7, Landsat 8, and Sentinel-2 were visualised against the surveyed (16 December 2020) high and low waterlines (Figure 10) to examine their accuracies. The high and low waterline were selected as the baselines, respectively, for validation against the extracted shorelines. Sixty-three (63) transects were cast at 50 m spacing (with a 170 m search distance) from respective baselines and clipped (to create transect intersects) to the shorelines and separate beach survey data for accuracy assessment.

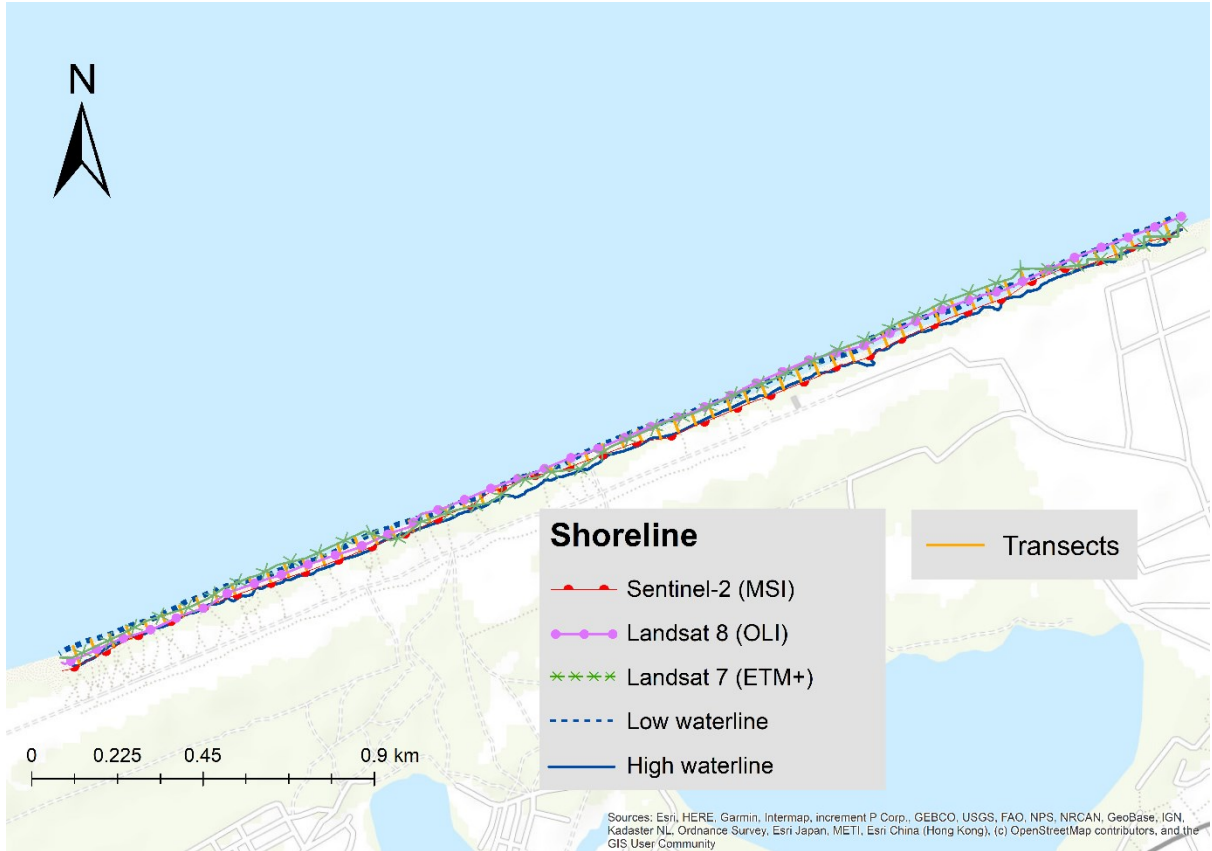


Figure 10. Comparison of shorelines derived from 2020 median composite (01 December 2020 to 31 December 2020) images of Landsat-7, Landsat-8, and Sentinel-2 using MNDWI.

The histogram of horizontal errors along transects (in meters) of all the SDS shows a mean ( $\mu$ ) error and standard deviation ( $\sigma$ ) of 20.9 m and 16.9 m, respectively, in comparison with the high waterline (Figure 11(a)). Similarly, a mean ( $\mu$ ) error and standard deviation ( $\sigma$ ) of -11.9 m and 16.9 m, respectively, were obtained for all the SDS in comparison with the position of the low water line (Figure 12(a)). The RMSE, mean error, and standard deviation of shorelines (from different satellite missions) were obtained with respect to the high and low waterline (Table 2). The RMSE and mean error values (Table 2) of shorelines derived from Landsat-7 and Landsat-8 images reveal a higher bias with the high waterline (Figure 11(b)) than the low water line (Figure 12(a)). On the other hand, RMSE and mean error (Table 2) values of the shoreline derived from the Sentinel-2 image show a lower bias with the high waterline (Figure 11(b)) compared to the low waterline (Figure 12(a)).

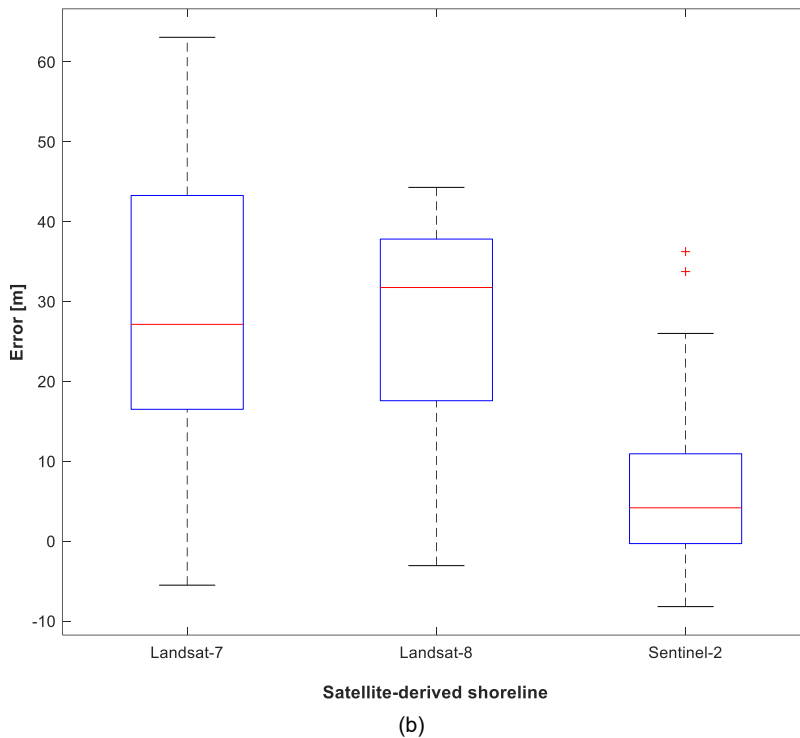
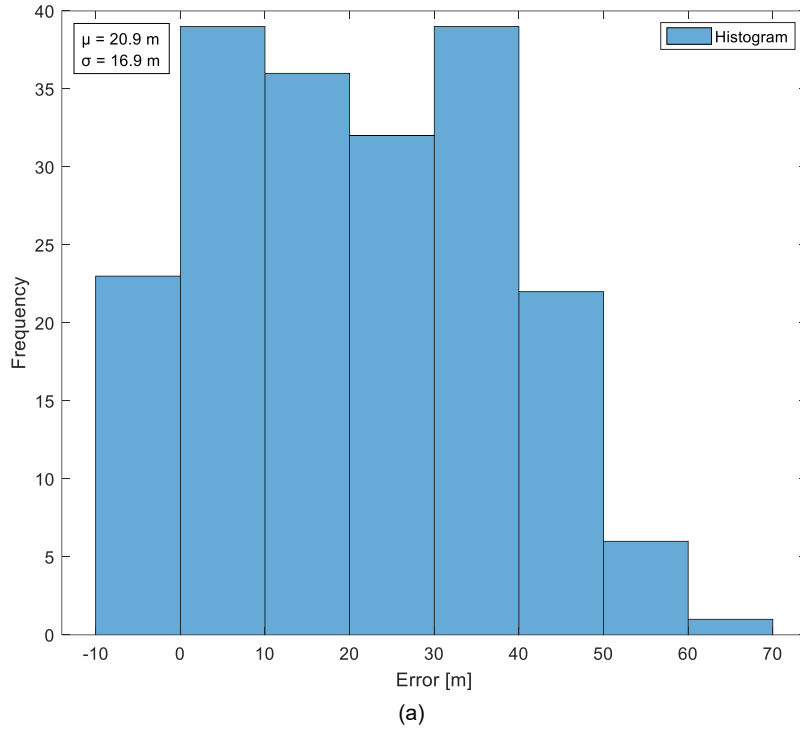
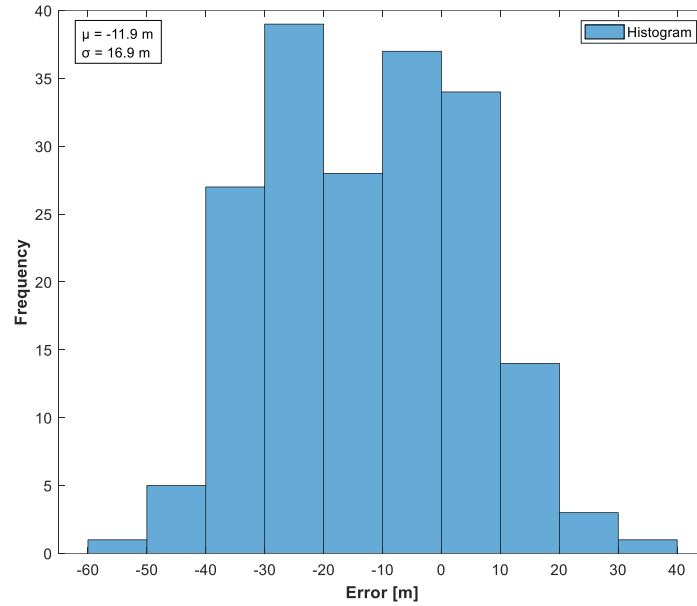
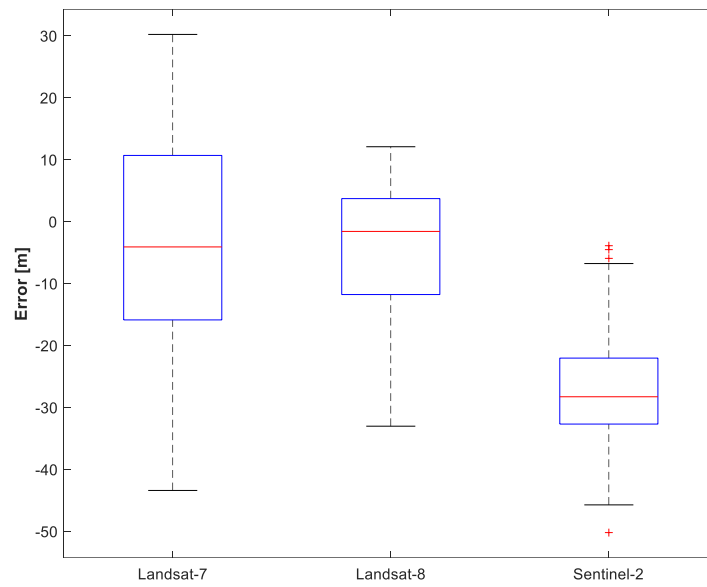


Figure 11. (a) Histogram of horizontal displacement (along transects) of satellite-derived shorelines from the high waterline (b) boxplot of horizontal displacement (along transects) of satellite-derived shorelines (from different satellite missions) from the high waterline.



(a)



Satellite-derived shoreline

(b)

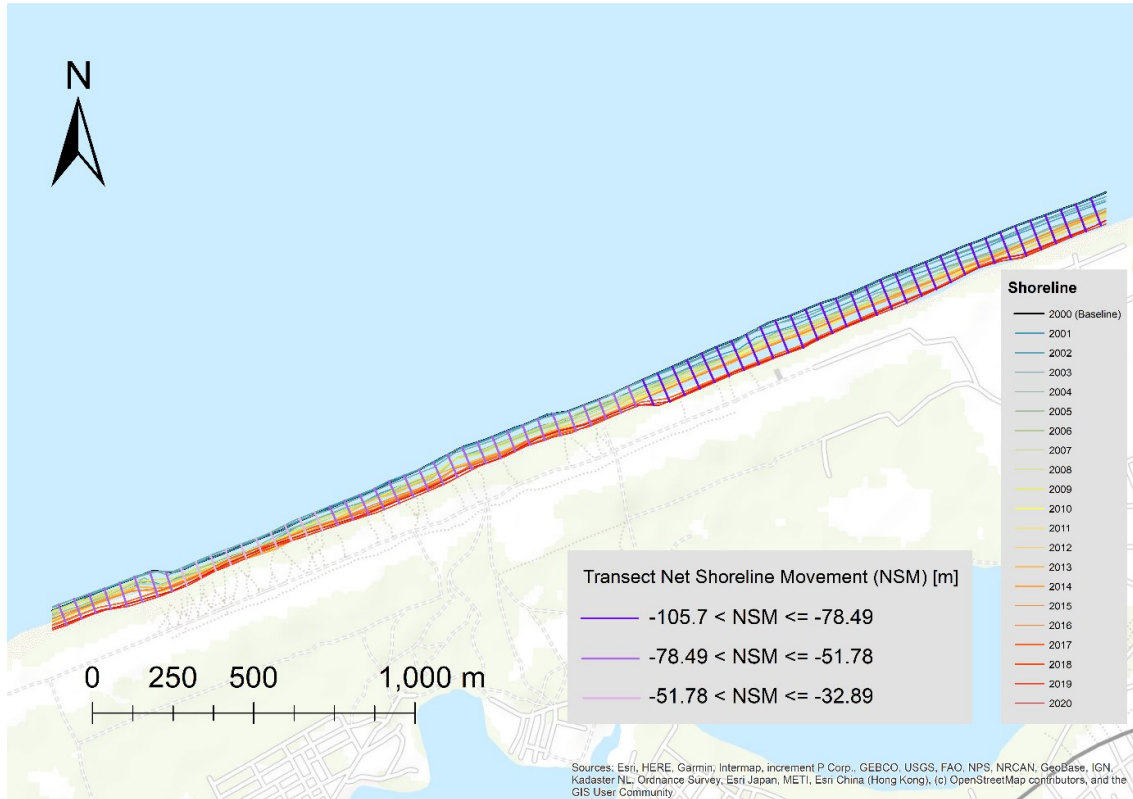
Figure 12. (a) Histogram of horizontal displacement (along transects) of satellite-derived shorelines from the low waterline (b) boxplot of horizontal displacement (along transects) of satellite-derived shorelines (from different satellite missions) from the low waterline.

Table 2. Validation of the satellite-derived shorelines (SDS) from different satellite missions relative to the high and low waterline

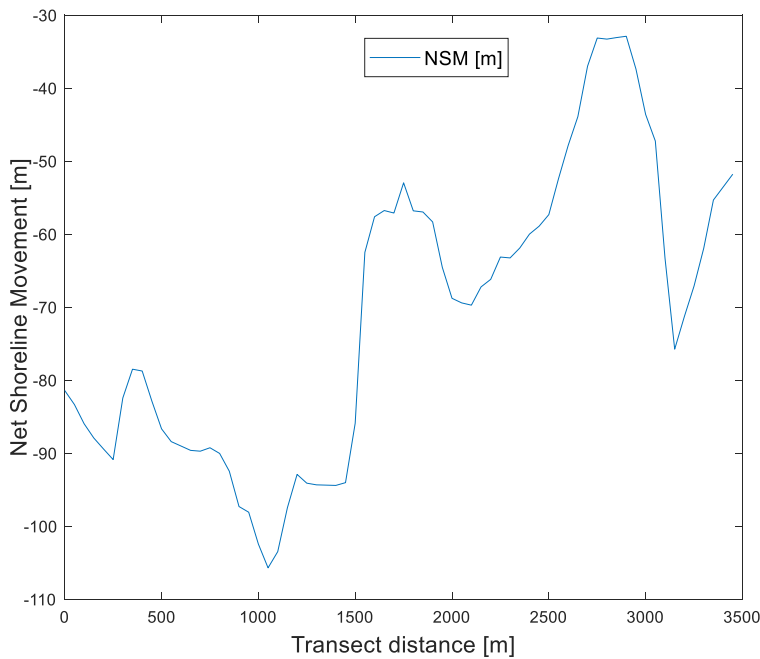
Satellite-derived shoreline	High waterline			Low waterline		
	RMSE [m]	Mean error [m]	Standard deviation [m]	RMSE [m]	Mean error [m]	Standard deviation [m]
Landsat-7	33.0	28.8	16.3	17.4	-4.2	17.0
Landsat-8	30.6	28.0	12.6	12.6	-4.7	11.8
Sentinel-2	11.5	5.9	10.0	28.6	-26.8	10.0

**4.1.2. Shoreline evolution**

Shorelines were derived from Landsat-7, Landsat-8, and Sentinel-2 images for 2000 – 2012, 2013 – 2015, and 2016 – 2020, respectively, using the MNDWI technique. The output highlights the shoreline changes over the 20-year study period. The Net Shoreline Movement (NSM) (Figure 13) derived with transects cast at 50 m intervals ranged from -32.89 m to -105.7 m with a mean of -71.2 m.



(a)



(b)

Figure 13. Net Shoreline Movement (NSM, in meters) of shorelines from 2000 - 2020 (a) across transects (b) scatter (line) plot.

The distance of the shorelines from the baseline (2000) across all transects (cast at 50 m intervals) (Figure 14) presents the retreating trend at a rate (Linear Regression Rate (LRR)) of -3.4 m/year that is statistically significant at 95% confidence interval (Mann Kendall test; p-value < 0) (Table 3) with a good coefficient of determination ( $R^2 = 0.63$ ).

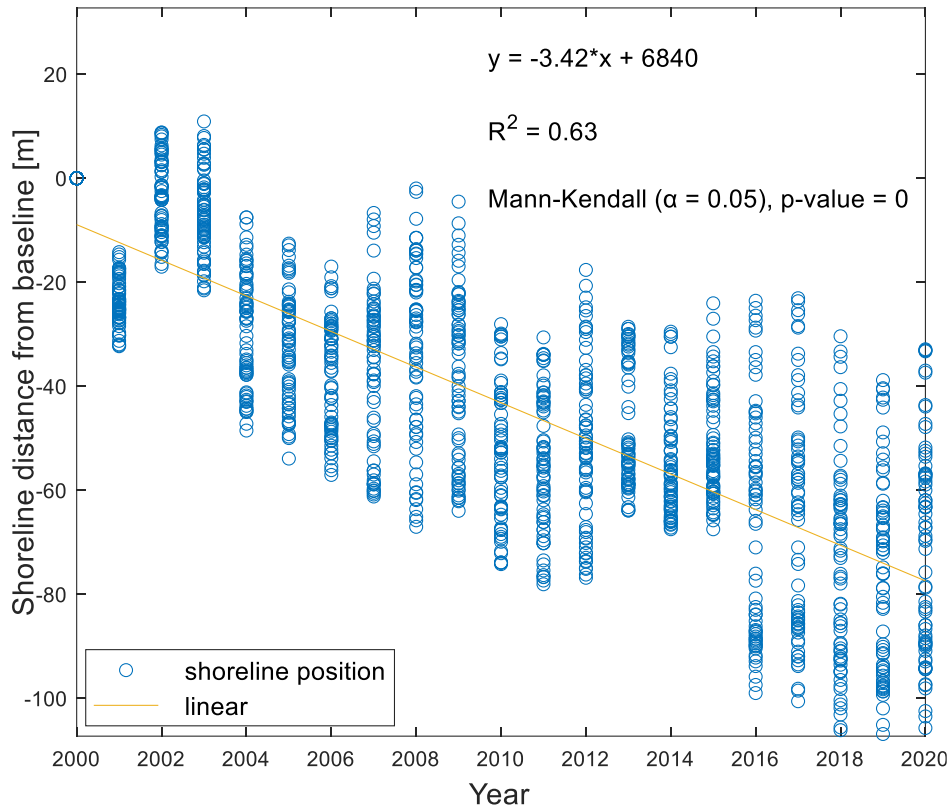


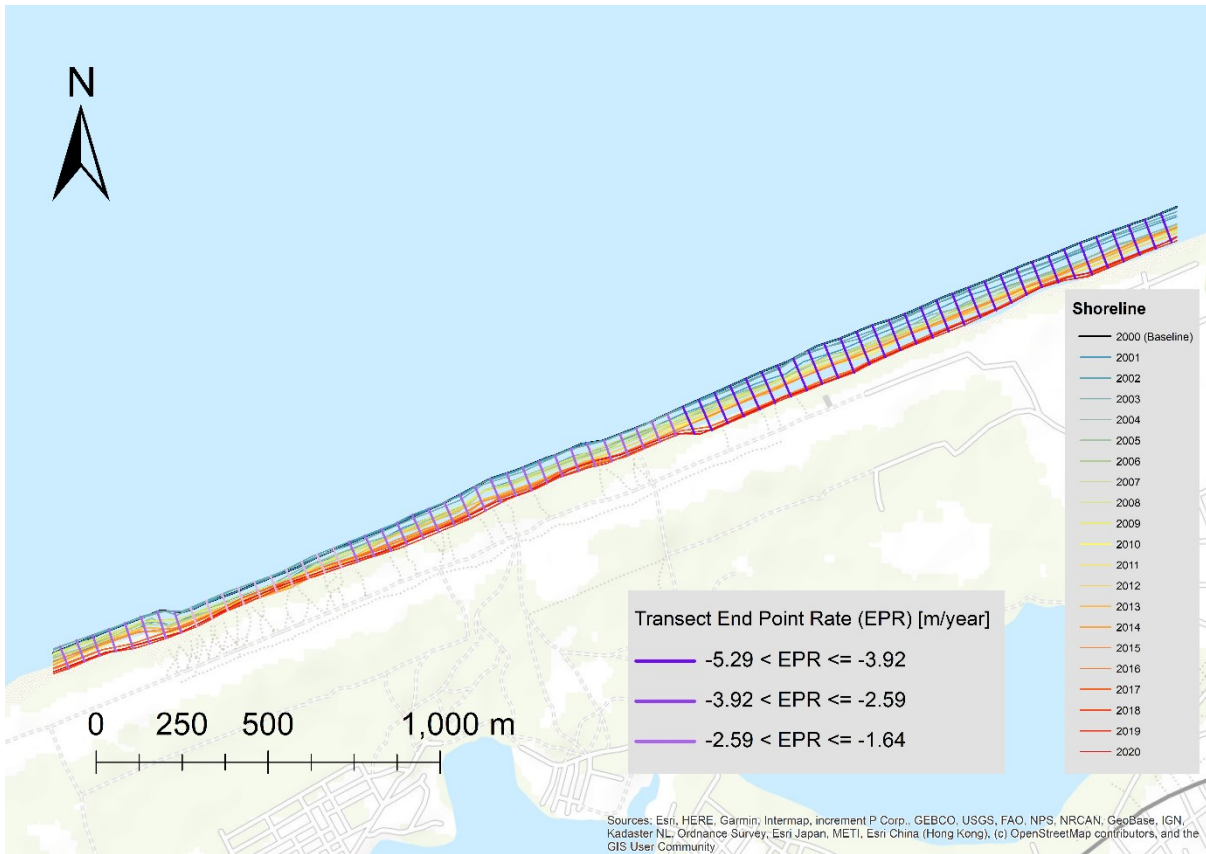
Figure 14. Scatter plot showing the Linear Regression Rate (LRR) of the shoreline from 2000 to 2020.

Table 3. Mann-Kendall test in detecting monotonic trends in shoreline retreat

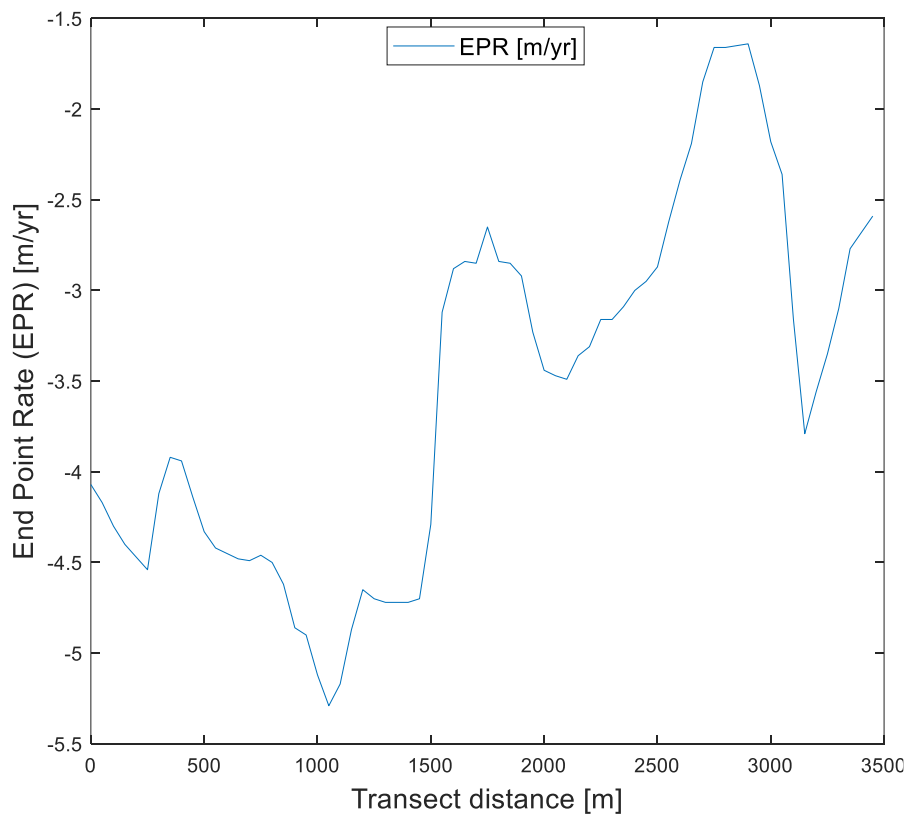
Parameter	Value
P-value	0*

\*Statistically significant at 5% ( $\alpha = 0.05$ ) significance level (p-value < 0.05)

The End Point Rate (EPR) (Figure 15) was also derived (from the ratio between the NSM (in meters) and the period (in years) between the oldest and the most recent shoreline position) with transects cast at 50 m intervals ranged from -1.64 m/year to -5.29 m/year with an average of -3.6 m/year.



(a)



(b)

Figure 15. End Point Rate (EPR, in m/year) of shorelines derived from 2000 – 2020 (a) across transects (b) scatter (line) plot.

#### 4.1.3. Forecasts of the shoreline position and vulnerability assessment

The forecast of the shoreline position over the next decade (10-year) and two decades (20-year) are shown in Figure 16. The DSAS uses the linear regression rate in predicting the future shoreline position. A 10 m uncertainty for each shoreline is set by USGS (Himmelstoss et al., 2018) as part of the forecast used to generate an uncertainty region that lies within a 95-percent confidence interval. An overlay of the forecasts of the future positions of the shoreline on the elevation map of the area was used to identify areas vulnerable to shoreline retreat (Figure 17). The degree of vulnerability decreases with an increase in elevation.

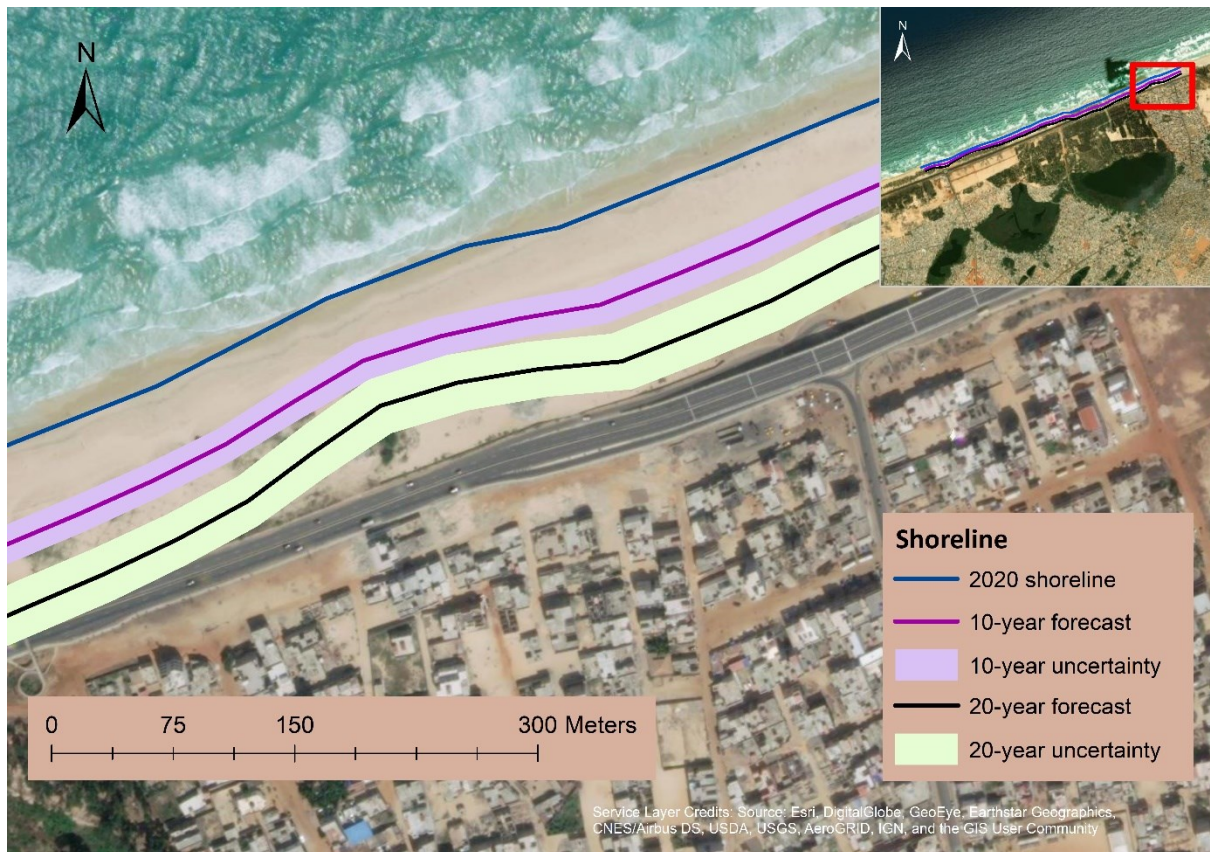


Figure 16. Forecasts (10- and 20-year) of the shoreline position.

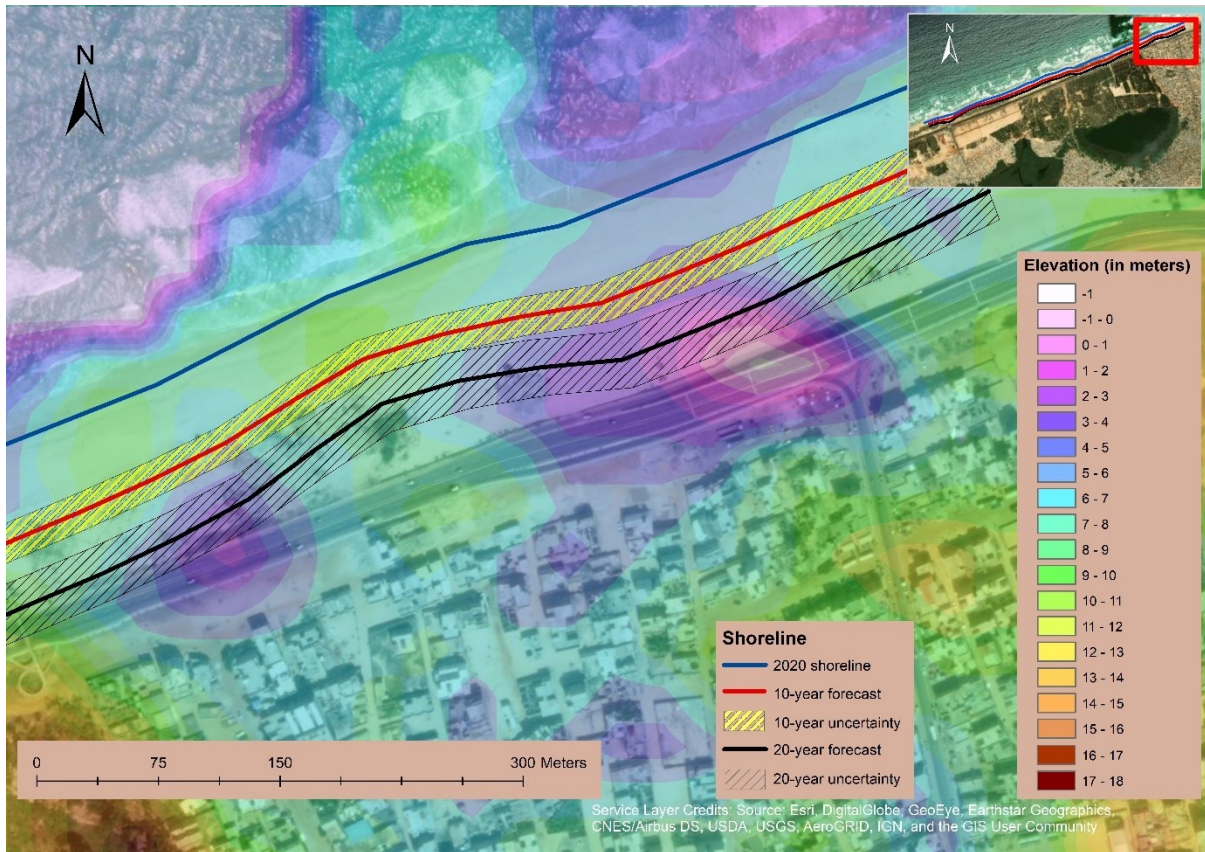


Figure 17. Elevation map covering part of the built-up area close to the shoreline

#### 4.1.4. Sea-level change

Monthly sea-level were obtained from daily tide gauge data. Annual mean (Figure 18) and annual maximum (extreme) (Figure 19) sea-level were computed afterward. The coast is microtidal (small tidal range (0 – 2 m)) (Hayes, 1975) with an annual mean and maximum sea-level rise of 2.4 cm (Figure 18) and 8.3 cm (Figure 19), respectively, between 2007 and 2020. The annual mean and annual maximum sea-level display an upward trend at a rate of 1.4 mm/year (Figure 18) and 4.4 mm/year (Figure 19). The Mann-Kendall test (Mann, 1945; Kendall, 1975) proved that the upward trend of the annual maximum sea-level was significant at a 5% significance level (with a low MAPE (1.72%) but low  $R^2$  (0.33)), but the upward trend of the annual mean sea-level was found not to be significant at 5% significant level (with  $R^2=0.13$ ) (Table 4).

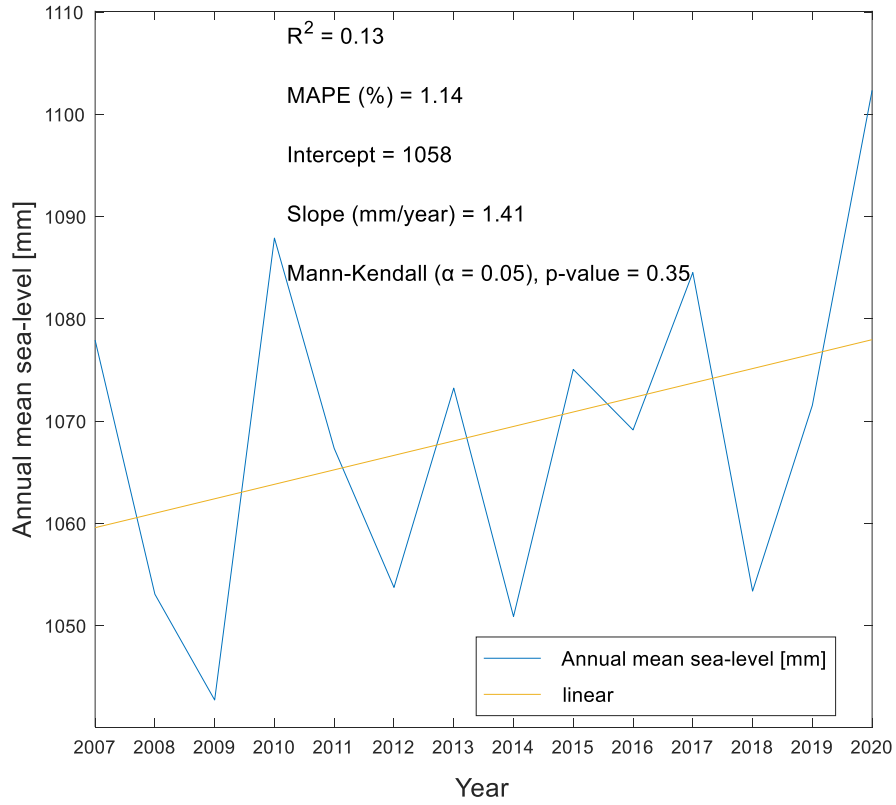


Figure 18. Annual mean sea-level from 2007 to 2020.

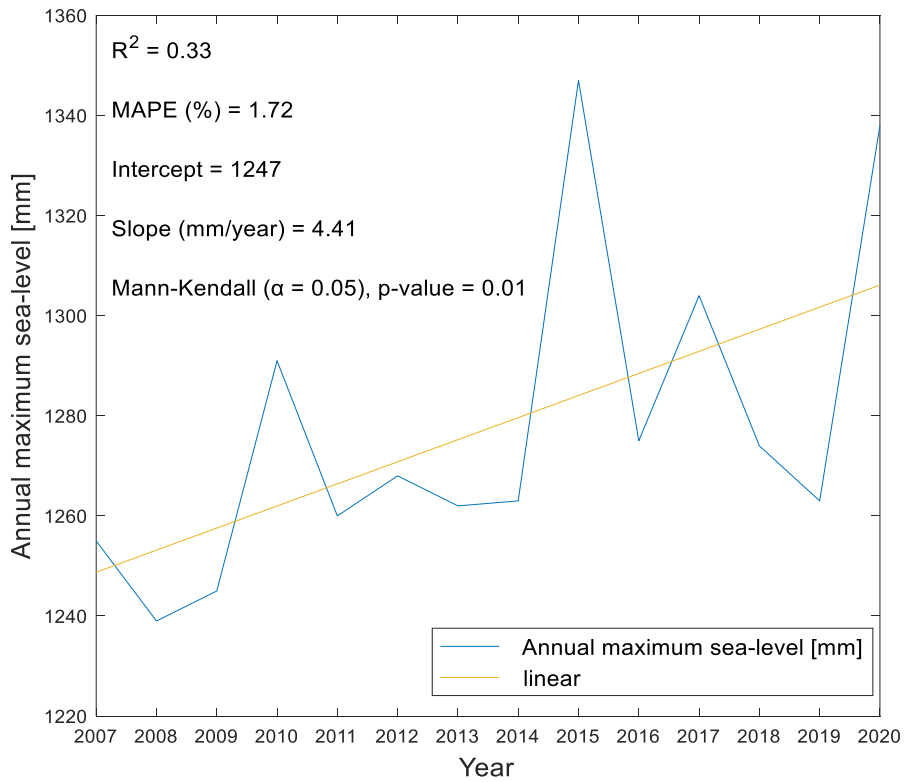


Figure 19. Annual maximum sea-level from 2007 to 2020.

**Table 4. Mann-Kendall test in detecting monotonic trends in sea-level time series**

Parameter	Annual mean sea-level	Annual maximum sea-level
Standard normal test statistic ( $Z_S$ )	0.93	2.47*
P-value	0.35	0.01**

\*Reject null hypothesis at 5% ( $\alpha = 0.05$ ) significance level ( $Z_S > 1.96$ )

\*\*Statistically significant at 5% ( $\alpha = 0.05$ ) significance level (P-value < 0.05)

#### 4.1.5. Sea-level change and shoreline displacement

The results of shoreline displacement and sea-level change are presented in Table 5. The cross-correlation of cross-shore displacement and sea-level rise (Table 6 and Table 7) yielded negative correlation coefficients ( $r$ ), revealing that the shoreline has a corresponding retreating response with increased sea level. However, without a lag, the correlation between all scenarios of sea-level and cross-shoreline displacement and coefficient of determination values were low ( $R^2 < 0.5$ ) and not significant at a 95-percent confidence interval. The optimum correlation between the annual minimum shoreline retreat and annual maximum sea-level (Table 7) was good ( $r = -0.75$  and  $R^2 > 0.5$ ), but the effect was significant (at a 95-percent confidence interval) after four years.

The linear regression model equation (equation(12)) of the scatter (line) plot between the annual mean shoreline displacement and the annual maximum sea-level rise (Figure 20) was not statistically significant ( $p = 0.12$ ,  $R^2 = 0.19$ , MAPE = 17.22%). However, it was selected to predict the future mean shoreline displacement because it had the highest correlation between cross-shore displacement and sea-level rise without a lag (lag (in years) = 0) ( $r = -0.44$  as shown in Table 7).

$$y = -0.19(x) + 185.8 \quad (12)$$

where  $y$ (criterion) = predicted future shoreline displacement (m),  $x$  (predictor) = sea level (mm),  $-0.19$  = coefficient of the predictor, and  $185.8$  = residual.

Table 5. Annual shoreline displacement and sea-level changes

Year	Annual mean sea-level [mm]	Annual maximum sea-level [mm]	Minimum shoreline distance from baseline [m]	Mean shoreline distance from baseline [m]	Maximum shoreline distance from baseline [m]
2007	1078	1255	-6.68	-36.78	-61.19
2008	1053	1239	-1.98	-33.13	-67.02
2009	1043	1245	-4.50	-38.12	-63.95
2010	1088	1291	-28.05	-52.55	-74.19
2011	1067	1260	-30.61	-54.72	-78.06
2012	1054	1268	-17.63	-50.71	-76.82
2013	1073	1262	-28.56	-48.01	-63.90
2014	1051	1263	-29.51	-54.69	-67.49
2015	1075	1347	-24.05	-51.64	-67.49
2016	1069	1275	-23.56	-65.90	-98.98
2017	1085	1304	-23.07	-65.61	-100.55
2018	1053	1274	-30.38	-74.16	-106.12
2019	1072	1263	-38.81	-76.50	-108.34
2020	1102	1338	-32.89	-71.2	-105.70

Table 6. Correlation between annual shoreline displacement and annual mean sea-level

Series	Minimum lag (years)	Correlation (r)	Coefficient of determination (R <sup>2</sup> )	Probability value (p-value)	Optimum number of lags (years)	Optimum correlation (r)	Coefficient of determination (R <sup>2</sup> )	Probability value (p-value)
Annual minimum shoreline displacement vs Annual mean sea- level	0	-0.41	0.17	0.14	3	-0.55	0.30	0.08*
Annual mean shoreline displacement vs Annual mean sea- level	0	-0.36	0.13	0.21	0	-0.36	0.13	0.21
Annual maximum shoreline displacement vs Annual mean sea- level	0	-0.34	0.11	0.24	0	-0.34	0.11	0.24

\*Significant at 90-percent confidence interval ( $p < 0.1$ )

Table 7. Correlation between annual shoreline displacement and annual maximum sea-level

Series	Minimum lag (years)	Correlation (r)	Coefficient of determination (R <sup>2</sup> )	Probability value (p-value)	Optimum number of lags (years)	Optimum correlation (r)	Coefficient of determination (R <sup>2</sup> )	Probability value (p-value)
Annual minimum shoreline displacement vs Annual maximum sea-level	0	-0.43	0.18	0.13	4	-0.75	0.56	0.01**
Annual mean shoreline displacement vs Annual maximum sea-level	0	-0.44	0.19	0.12	4	-0.62	0.39	0.06*
Annual maximum shoreline displacement vs Annual maximum sea-level	0	-0.33	0.11	0.24	6	-0.66	0.44	0.08*

\*\*significant at 95-percent confidence interval ( $p < 0.05$ ) \*Significant at 90-percent confidence interval ( $p < 0.1$ )

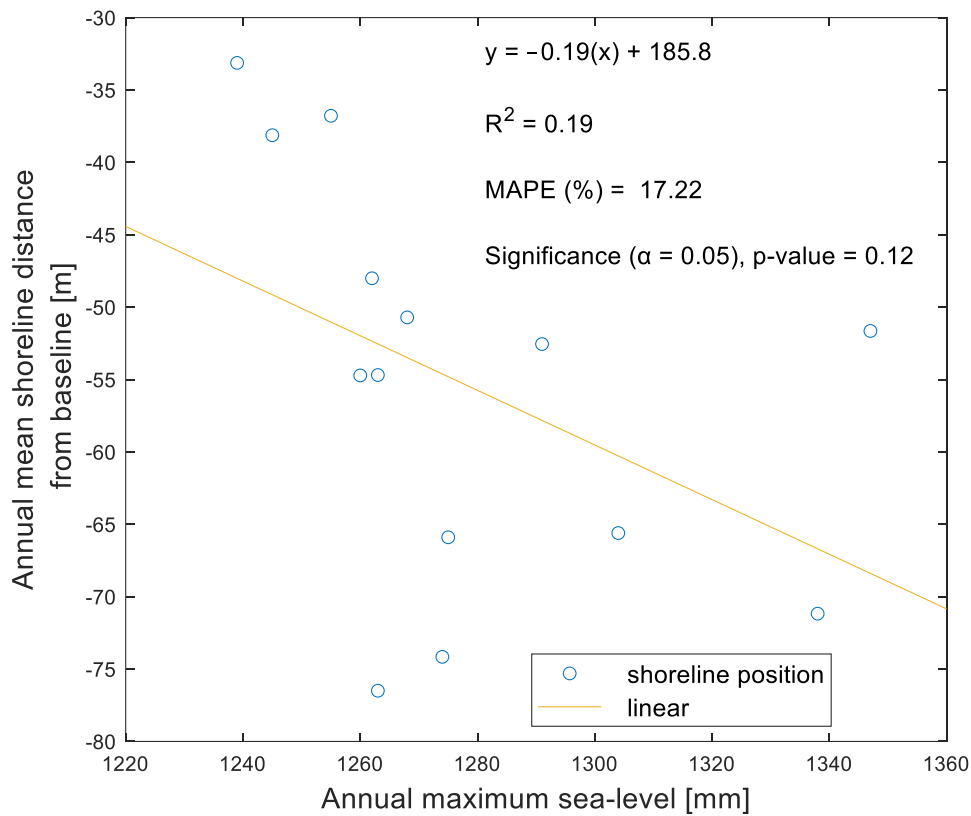


Figure 20. Scatter plot of annual mean shoreline displacement (m) and annual maximum sea-level (mm)

## 4.2. Discussion

### 4.2.1. Shoreline extraction

Shoreline extraction using satellite data is a complicated and time-consuming task. The major challenge faced by most image segmentation and edge detection techniques arises due to insufficient intensity distinction in areas covered by water and land (H. Liu & Jezek, 2004b) because water has a relatively low reflectance in the visible spectrum (Malinowski, Groom, Schwanghart, & Heckrath, 2015). Therefore, a slightly wet shore will lead to a wrong delineation (Levy, Nolin, Fountain, & Head, 2014). The accuracy assessment of the shoreline extraction techniques applied in this study was based on visual interpretation and comparison with the source (original) satellite images. MNDWI approach displayed an excellent segmentation of the land and sea boundary in this study. The method suppresses land and vegetation and creates a binary image that delineates the shoreline (Xu, 2006). Applying MNDWI in shoreline extraction was satisfactory on Landsat-7, Landsat-8, and Sentinel-2 median composite images (Figure 5(a), Figure 6(a), Figure 7(a)).

The adaptive thresholding technique proves to delineate the line separating water and land (Figure 6(b), Figure 7(b)). However, the technique displays limitations (Figure 5(b)) observed due to the grouping of land and water (sea) pixels in the same cluster.

Canny Edge Detection identified two edges when applied to the 2020 Sentinel-2 median composite image creating uncertainty about the shoreline position (Figure 9). The technique failed to identify the shoreline

from the Sentinel-1 median composite image. It rather returned edges between vegetation and sand around the beach because the change in the intensity (sigma nought) was more abrupt compared to the land-sea boundary (Figure 8). The MIR band of the Sentinel-2 image presents apparent differences in intensity between land and water (Figure 9(a)), which aided better identification of the shoreline (Pardo-Pascual et al., 2018) as compared to the Sentinel-1 image. The technique identified two edges because pixels containing both land and sea created a fuzzy shoreline that led the method to detect two edges due to the intensity changes within those pixels (Figure 9(a)). However, the edges extracted from Sentinel-2 were also not ultimately continuous because some locations had little or no change in intensity.

Shoreline extracted with four (4) weeks median composite images (centred around the beach survey date) using MNDWI were validated with the beach survey (high and low waterline) data. The differences in the number of images (due to the satellite revisit time differences) in the median composites of Landsat and Sentinel (Sentinel-2) account for the variation in bias in connection with the high and low waterline (Table 2). Validation of the shorelines returned a mean ( $\mu$ ) error of 20.9 m and -11.9 m with respect to the high and low waterline, respectively. The use of median composite images (an image composed from the median pixel value of all the images in a composite) used in extracting the shorelines also contributed to the bias obtained between the SDS and the in situ (beach survey) data because the positions of shorelines obtained (from the median composite image) are not instantaneous (Dimosthenis Traganos et al., 2018).

#### **4.2.2. Sea-level rise and shoreline evolution**

GMSL rise triggered by climate change is caused by the increase in ocean water and ocean mass (from melting glaciers) due to global warming (Oppenheimer et al., 2019). The Intergovernmental Panel on Climate Change (IPCC) Fifth Assessment Report (AR5) GMSL projection considered the contributions from physical processes in the derivation of a possible 66% probability value of GMSL rise of 0.52 – 0.98 m in the uncontrolled increase in greenhouse gas emissions scenario (Representative Concentration Pathway [RCP] 8.5) by 2100 (Church et al., 2013; Horton et al., 2020). However, most publications since 2013 linked to the high emission scenario (RCP 8.5) made projections of GMSL rise greater than 1 m by 2100 (Garner et al., 2018, Horton et al., 2020), with many reporting the likelihood of an increase higher than 2m (Kopp et al., 2017; Wong, Bakker, & Keller, 2017).

The shoreline evolution in the region of interest (covering Gadaye and Malika beaches in Dakar) from 2000 to 2020 reveals a retreating trend (average NSM and EPR of -71.2 m of -3.6m/year, respectively). The negative correlation between sea-level rise (SLR) and shoreline retreat (Table 6 and Table 7) provides insight into the potential SLR has on shoreline displacement. However, the results point out that the effect of sea-level rise on shoreline retreat might not be instantaneous but become significant over the long term, which agrees with the Bruun rule (Bruun, 1954, 1962, 1988).

Thior et al. (2019) assessed the northern Lower Casamance's (Senegal) coastal dynamics and the southern Gambia from 1968 to 2017. Between 1968 and 1986, the entire extent of the study area was dominated by accretion (-0.33 m/year in the north and +6.01 m/year in the south) while an erosive trend (-4.76 m/year

and -4.57 m/year in the north and south, respectively) was observed between 1986 and 2004. The erosive (-3.75 m/year in the north and -2.03 m/year in the south) pattern (attributed to SLR) progressed from 2004 to 2017. Bakhoum et al. (2017) carried out coastline mobility assessment in Goree Island (Dakar, Senegal) from 1942 to 2011. The results they obtained show that the shoreline retreated (-4 m) at an average rate of -0.16 m/year and -0.06 m/year from 1942 and 1966 and 1966 to 2011, respectively. The island was identified to be vulnerable to sea-level rise between 1942 and 1966, but the construction of protective structures (1979 – 1981) to control flooding led to the reduction in the rate of retreat (-0.06 m/year) recorded between 1966 to 2011.

SLR poses as a ‘substantive driver,’ with extreme events, tides, changes in wave patterns, and human intervention usually portrayed as the principal drivers of coastal flooding (Grady, Moore, Storlazzi, Elias, & Reidenbach, 2013; Albert et al., 2016; Pollard, 2018). In addition to global and regional sea-level variations, vertical ground motions can significantly promote local promote sea-level changes (Cozannet et al., 2015). Subsidence ascribed to shrinkage of aquifer-system due to groundwater extraction accounted for about 85% (of the 0.7 m) relative SLR since 1909, and an extra 1.9 m is predicted by 2100 (Y. Liu, Li, Fasullo, & Galloway, 2020).

Instantaneous events such as storm surges (temporal extremes of sea level) can cause abrupt and non-reversible shoreline changes. These events can contribute to the long-term shoreline evolution (Sagne et al., 2020). The open-ocean coast of Dakar is also exposed to the impacts of these natural processes. Typical strong and constant swells in Dakar (with an NNW – SE orientation) and strong eroding waves induce the shoreline’s landward movements (Sane & Yamagishi, 2004).

Sagne et al. (2020) assessed the morphological impacts of swells in Dakar (Malibu, Gadaye, and Malika) between October and November 2018. They found out that swells have a significant erosive effect which was attributed to low topography and unsheltered setting of the environment. The slopes of Gadaye, Malika, and Malibu beaches changed (decreased) from 7.39% to 5.91%, 7.28% to 3.78%, and 7.38% to 6.15%, respectively. Gadaye and Malika beaches’ foreshore widened by 11.8 m and 42.5 m, respectively, whereas Malibu beach reduced by 7.5 m (due to underwater beach erosion).

The Bruun rule (Bruun, 1954, 1962, 1988) postulates that the shape of the active part of the profile perpendicular to the shore is maintained over the long term and rises with sea-level rise. The active profile moves upward when there is a source of sand supply (Figure 21). The profile extends to a depth known as “closure depth.” Beyond the closure depth, the sand motion is minimal. The Bruun rule assumes that the sand is transported from the shore, leading to shoreline recession. Equation (13 presents the relationship between shoreline change ( $\Delta X$ ), sea-level rise ( $\Delta S$ ), length of active profile ( $W_*$ ), beach berm height ( $B$ ), and closure depth ( $h_*$ ) with the assumption that  $\Delta X \ll W_*$  and  $\Delta S \ll h_*$  (Dean, 1987).

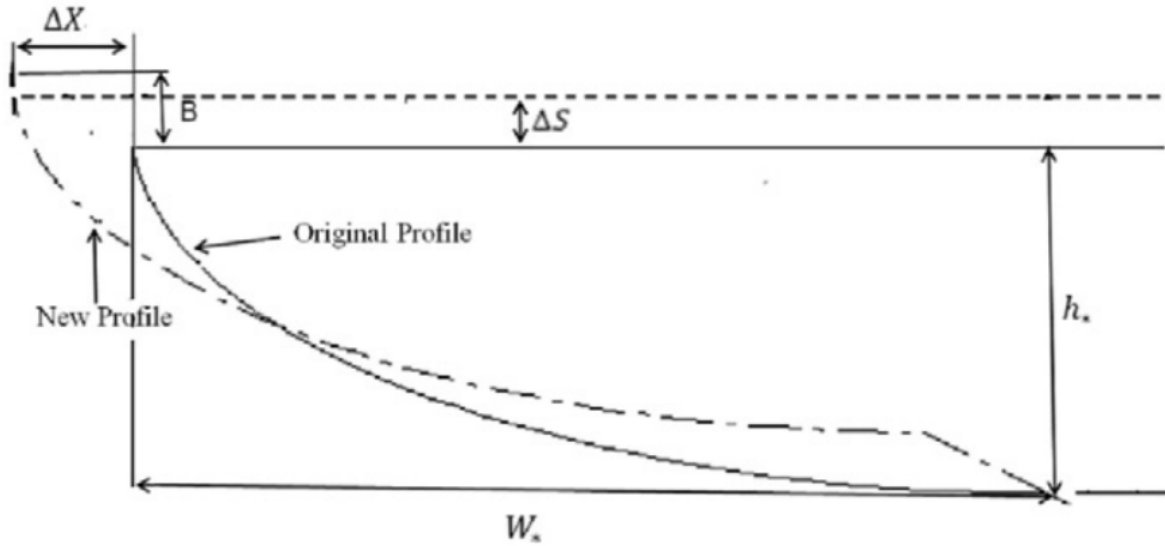


Figure 21. Active profile response to sea-level rise according to the Bruun rule (Source: (Dean & Houston, 2016))

$$\Delta X = -\Delta S \left( \frac{W_*}{h_* + B} \right) \quad (13)$$

The high concentration of industries and rapid population growth (3% per year) in the study area (Dakar) has adversely affected the open-ocean coast in the past years. The strong eroding waves (especially during the rough-sea season (December to May)) and wind force supply sand to the beach, but the local populations remove a large volume of the sand as construction material. Human alteration of the sediment supply process contributes to the erosion of the shoreline in the area (Sane & Yamagishi, 2004). The induced (natural and human) net sediment imbalance decreases the elevation of the dunes, which allows such locations to be flooded with seawater (Filho et al., 2021).

Regardless of the rapid population growth and development in Dakar, the city has not been affected by vertical ground motions greater than 1 mm/year. Subsidence recorded after 2000 was attributed to land reclamation works. Notwithstanding, these accounts of ground motions did not affect the tide gauge observations (Cozannet et al., 2015).

Considering the high emission scenario (RCP 8.5) of SLR projection (> 1 meter by 2100), the annual maximum sea level in the study area is likely to rise from 1338 mm (in 2020) (Table 5) to greater or equal to 2338 mm. Applying the projected sea-level value (2338 mm) in equation (12), the predicted future shoreline displacement (m) will be equal to -258.4 m (187.2 m landward from mean shoreline position in 2020). This prediction implies that the shoreline is likely to retreat to the road (Figure 17) in the study area (especially areas with elevation less than 1m).

## 5. CONCLUSION AND RECOMMENDATIONS

### 5.1. Conclusion

This research assessed techniques (Modified Normalized Difference Water Index, Adaptive thresholding, and Canny Edge Detection Algorithm) of shoreline extraction from Landsat-7 (Enhanced Thematic Mapper), Landsat-8 (Operational Land Imager), Sentinel-1 (Synthetic Aperture Radar), and Sentinel-2 (Multispectral Instrument) median composite images. The rate of shoreline change statistics from 2000 to 2020 was evaluated with the Digital Shoreline Analysis System (DSAS). The DSAS calculates future positions of the shoreline for the next 10 and 20 years using the linear regression rate. Finally, the study also explored the influence of sea-level rise on shoreline change and identified areas vulnerable to shoreline retreat. The discoveries from the study are as follows:

- ❖ Modified Normalized Difference Water Index (MNDWI) was more reliable in delineating the shoreline than adaptive thresholding and Canny Edge Detection techniques.
- ❖ Adaptive thresholding technique displayed limitations observed due to the grouping of land and water (sea) pixels in the same cluster.
- ❖ Canny Edge Detection applied to Sentinel-1 annual median composite image failed to delineate the shoreline but returned the edge between vegetation and sand around the beach instead due to the abrupt change in intensity (sigma nought) observed compared to the land-sea boundary.
- ❖ Validation of the shorelines extracted from satellite data (Landsat-7, Landsat-8, and Sentinel-2) using MNDWI revealed that their positions fell within the high and low waterline. The accuracy assessment returned an overall mean ( $\mu$ ) error of 20.9 m (seaward bias with RMSE not exceeding 33.0 m) and -11.9 m (landward bias with RMSE not exceeding 28.6m) with respect to the high and low waterline, respectively.
- ❖ The shoreline evolution in the region of interest (an open coast in Dakar) from 2000 to 2020 reveals an erosive trend with an average Net Shoreline Movement (NSM) and End Point Rate (EPR) of -71.2 m of -3.6 m/year, respectively.
- ❖ The negative correlation between sea-level rise (SLR) and shoreline retreat provides insight into the potential SLR has on shoreline displacement.
- ❖ Applying the linear regression model equation obtained linking shoreline displacement and sea-level, the shoreline is likely to retreat by 187.2 m landward from the 2020 shoreline position by 2100 (considering the high emission scenario (RCP 8.5) of SLR projection (> 1 m by 2100)).

### 5.2. Recommendations

- ❖ For a near real-time accuracy assessment of satellite-derived shoreline, the beach survey should be carried out at the same time the satellite passes over the area of interest.

- ❖ The results reveal that the effect of sea-level rise on shoreline retreat might not be instantaneous but become significant over the long term.
- ❖ For further research, the movement of the sediments should be monitored and quantified over the long term relative to the changes in the sea level to gain proper insight into how the shoreline changes in response to sea-level rise.

## LIST OF REFERENCES

- Aedla, R., Dwarakish, G. S., & Reddy, D. V. (2015). Automatic Shoreline Detection and Change Detection Analysis of Netravati-GurpurRivermouth Using Histogram Equalization and Adaptive Thresholding Techniques. *Aquatic Procedia*, 4(Icwrcoe), 563–570. <https://doi.org/10.1016/j.aqpro.2015.02.073>
- Albert, S., Saunders, M. I., Chris, M., Albert, S., Leon, J. X., Grinham, A. R., ... Gibbes, B. R. (2016). Interactions between sea-level rise and wave exposure on reef island dynamics in the Solomon Islands Interactions between sea-level rise and wave exposure on reef island dynamics in the Solomon Islands. *Environmental Research Letters*, 11(054011). <https://doi.org/10.1088/1748-9326/11/5/054011>
- Anderberg, M. R. (1973). Cluster Analysis for Applications. In *Cluster Analysis for Applications*. <https://doi.org/10.1016/c2013-0-06161-0>
- Armaroli, C., Ciavola, P., Balouin, Y., & Gatti, M. (2006). An integrated study of shoreline variability using GIS and ARGUS techniques. *Journal of Coastal Research*, (39 SPEC. ISSUE), 473–477. Retrieved from <https://www.researchgate.net/publication/231582634>
- Armstrong, B. J. S., & Collopy, F. (1992). Error Measures For Generalizing About Forecasting Methods: Empirical Comparisons By J. Scott Armstrong and Fred Collopy Reprinted with permission form. *International Journal of Forecasting*, 8(1), 69–80. Retrieved from [http://papers.ssrn.com/sol3/papers.cfm?abstract\\_id=662701](http://papers.ssrn.com/sol3/papers.cfm?abstract_id=662701)
- Bakhoun, P. W., Ndour, A., Niang, I., Sambou, B., Traore, V. B., Diaw, A. T., ... Ndiaye, M. L. (2017). Coastline Mobility of Goree Island ( Senegal ), from 1942 to 2011. *Marine Science*, 7(1), 1–9. <https://doi.org/10.5923/j.ms.20170701.01>
- Bamler, R. (2000). Principles of synthetic aperture radar. *Surveys in Geophysics*, 21(2–3), 147–157. <https://doi.org/10.1023/A:1006790026612>
- Bhatia, S. K. (2004). Adaptive K-Means Clustering. *FLAIRS Conference*. Retrieved from <https://www.aaai.org/Papers/FLAIRS/2004/Flairs04-119.pdf>
- Bird, E. C. P. (1996). Coastal Erosion and Rising Sea-Level. In Milliman J.D. & H. B.U. (Eds.), *Sea-Level Rise and Coastal Subsidence. Coastal Systems and Continental Margins* (pp. 87–88). Retrieved from [https://doi.org/10.1007/978-94-015-8719-8\\_5](https://doi.org/10.1007/978-94-015-8719-8_5)
- Boak, E. H., & Turner, I. L. (2005). Shoreline Definition and Detection: A Review. *Journal of Coastal Research*, 214(214), 688–703. <https://doi.org/10.2112/03-0071.1>
- Bruun, P. (1954). *Coast erosion and the development of beach profiles*. Retrieved from [https://books.google.com/books?hl=en&lr=&id=I1YOmK4aYI0C&oi=fnd&pg=PA3&ots=6dIQ3i40r-&sig=JMfz9O8QYeK1WSFjzqufUB\\_ZOS0](https://books.google.com/books?hl=en&lr=&id=I1YOmK4aYI0C&oi=fnd&pg=PA3&ots=6dIQ3i40r-&sig=JMfz9O8QYeK1WSFjzqufUB_ZOS0)
- Bruun, Per. (1962). Sea-Level Rise as a Cause of Shore Erosion. *Journal of the Waterways and Harbors Division*, 88(1), 117–130. <https://doi.org/10.1061/jwheau.0000252>
- Bruun, Per. (1988). *The Bruun Rule of Erosion by Sea-Level Rise: A Discussion on Large-Scale Two-and Three-Dimensional Usages* m~ ••~.
- Buono, A., Nunziata, F., Mascolo, L., & Migliaccio, M. (2014). A Multipolarization Analysis of Coastline Extraction. *IEEE Journal of Selected Topics in Applied Earth Observation and Remote Sensing*, 7(7), 2811–2820. Retrieved from 10.1109/JSTARS.2014.2320366
- Canny, J. (1986). A Computational Approach to Edge Detection. *IEEE Transactions on Pattern Analysis and Machine Intelligence*, Pami-8(6), 679–698. Retrieved from <https://ieeexplore.ieee.org/stamp/stamp.jsp?tp=&arnumber=4767851>
- Chander, G., Markham, B. I., & Helder, D. L. (2009). Summary of current radiometric calibration coefficients for Landsat MSS, TM, ETM+, and EO-1 ALI sensors - ScienceDirect. *Remote Sensing of Environment*, 113, 893–903. <https://doi.org/http://dx.doi.org/10.1016/j.rse.2009.01.007>
- Cheng, C. L., Shalabh, & Garg, G. (2014). Coefficient of determination for multiple measurement error models. *Journal of Multivariate Analysis*, 126, 137–152. <https://doi.org/10.1016/j.jmva.2014.01.006>
- ChenthamilSelvan, S., Kankara, R. S., & Rajan, B. (2014). Assessment of shoreline changes along Karnataka coast, India using GIS & remote sensing techniques. *Indian Journal of Geo-Marine Sciences*, 43(7), 1286–1291.
- Church, J. A., Clark, P. U., Cazenave, A., Gregory, J. M., Jevrejeva, S., Levermann, A., ... Unnikrishnan, A. S. (2013). *Sea level rise by 2100*. 5–6. Retrieved from [http://nora.nerc.ac.uk/id/eprint/504359/1/Science\\_Letter\\_final.pdf](http://nora.nerc.ac.uk/id/eprint/504359/1/Science_Letter_final.pdf)

- Church, J. A., & White, N. J. (2011). Sea-Level Rise from the Late 19th to the Early 21st Century. *Surveys in Geophysics*, 32(4–5), 585–602. <https://doi.org/10.1007/s10712-011-9119-1>
- Clemens, K., Niang-diop, I., Nicholls, R. J., Dennis, K. C., Niang-diop, I., & Nicholls, R. J. (1995). Sea-Level Rise and Senegal: Potential Impacts and Consequences. *Journal of Coastal Research*, (14), 243–261. Retrieved from <https://www.jstor.org/stable/25735711>
- Cozannet, G. Le, Raucoules, D., Wöppelmann, G., Garcin, M., Sylva, S. Da, Meyssignac, B., ... Franck, L. (2015). Vertical ground motion and historical sea-level records in Dakar (Senegal). *Environmental Research Letters*. <https://doi.org/10.1088/1748-9326/10/8/084016>
- de Boer, W., Mao, Y., Hagenaars, G., de Vries, S., Slinger, J., & Vellinga, T. (2019). Mapping the sandy beach evolution around seaports at the scale of the African continent. *Journal of Marine Science and Engineering*, 7(5). <https://doi.org/10.3390/jmse7050151>
- de Myttenaere, A., Golden, B., Le Grand, B., & Rossi, F. (2016). Mean Absolute Percentage Error for regression models. *Neurocomputing*, 192, 38–48. <https://doi.org/10.1016/j.neucom.2015.12.114>
- Dean, R. G. (1987). Additional sediment input to the nearshore region. *Shore & Beach*, 55(3–4, Jul.-Oct. 1987), 76–81.
- Dean, R. G., & Houston, J. R. (2016). Determining shoreline response to sea level rise. *Coastal Engineering*, 114, 1–8. <https://doi.org/10.1016/j.coastaleng.2016.03.009>
- Demir, N., Oy, S., Erdem, F., Seker, D. Z., & Bayram, B. (2017). Integrated Shoreline Extraction with use of RASAT MS and Sentinel-1A SAR images. *ISPRS Annals of the Photogrammetry, Remote Sensing and Spatial Information Sciences*, 4(2W4), 445–449. <https://doi.org/10.5194/isprs-annals-IV-2-W4-445-2017>
- Dewangan, S., & Kumar Sharma, A. (2017). Image Smoothing and Sharpening using Frequency Domain Filtering Technique. *International Journal of Emerging Technologies in Engineering Research*, 5(4), 169–174.
- Dimosthenis Traganos, Poursanidis, D., Aggarwal, B., Chrysoulakis, N., & Reinartz, P. (2018). Estimating Satellite-Derived Bathymetry (SDB) with the Google Earth Engine and Sentinel-2. *Remote Sensing*, 10(859), 1–18. <https://doi.org/10.3390/rs10060859>
- Douglas, E. M., Vogel, R. M., & Kroll, C. N. (2000). Trends in floods and low flows in the United States: Impact of spatial correlation. *Journal of Hydrology*, 240(1–2), 90–105. [https://doi.org/10.1016/S0022-1694\(00\)00336-X](https://doi.org/10.1016/S0022-1694(00)00336-X)
- El-Deen Taha, L. G., & Elbeih, S. F. (2010). Investigation of fusion of SAR and Landsat data for shoreline super resolution mapping: The northeastern mediterranean sea coast in Egypt. *Applied Geomatics*, 2(4), 177–186. <https://doi.org/10.1007/s12518-010-0033-x>
- Ericson, J. P., Vörösmarty, C. J., Dingman, S. L., Ward, L. G., & Meybeck, M. (2006). Effective sea-level rise and deltas: Causes of change and human dimension implications. *Global and Planetary Change*, 50(1–2), 63–82. <https://doi.org/10.1016/j.gloplacha.2005.07.004>
- Fenster, M. S., Dolan, R., & Morton, R. A. (2001). Coastal storms and shoreline change: Signal or noise? *Journal of Coastal Research*, 17(3), 714–720.
- Filho, W. L., Hunt, J., Lingos, A., Platje, J., Vieira, L. W., Will, M., & Gavriletea, M. D. (2021). The unsustainable use of sand: Reporting on a global problem. *Sustainability*, 13(6), 1–16. <https://doi.org/10.3390/su13063356>
- Filipponi, F. (2019). Sentinel-1 GRD Preprocessing Workflow †. *3rd International Electronic Conference on Remote Sensing*, 1–4. <https://doi.org/10.3390/ECRS-3-06201>
- Fu, K. S., & Mui, J. K. (1981). A survey on image segmentation. *Pattern Recognition*, 13(1), 3–16. [https://doi.org/10.1016/0031-3203\(81\)90028-5](https://doi.org/10.1016/0031-3203(81)90028-5)
- Garner, A. J., Weiss, J. L., Parris, A., Kopp, R. E., Overpeck, J. T., & Horton, B. P. (2018). Evolution of 21st Century Sea Level Rise Projections Earth's Future. *Earth's Future*, 1603–1615. <https://doi.org/10.1029/2018EF000991>
- Gens, R. (2010). *Remote sensing of coastlines: detection, extraction and monitoring*. 1161. <https://doi.org/10.1080/01431160902926673>
- Ghosh, M. K., Kumar, L., & Roy, C. (2015). Monitoring the coastline change of Hatiya Island in Bangladesh using remote sensing techniques. *ISPRS Journal of Photogrammetry and Remote Sensing*, 101, 137–144. <https://doi.org/10.1016/j.isprsjprs.2014.12.009>
- Gocic, M., & Trajkovic, S. (2013). Analysis of changes in meteorological variables using Mann-Kendall and Sen's slope estimator statistical tests in Serbia. *Global and Planetary Change*, 100, 172–182. <https://doi.org/10.1016/j.gloplacha.2012.10.014>
- Gonzalez, R. C., Woods, R. E., & Hall, P. (2002). *Digital Image Processing*. New Jersey: Patience Hall.

- Grady, A. E., Moore, L. J., Storlazzi, C. D., Elias, E., & Reidenbach, M. A. (2013). The influence of sea level rise and changes in fringing reef morphology on gradients in alongshore sediment transport. *Geophysical Research Letters*, *40*(April), 3096–3101. <https://doi.org/10.1002/grl.50577>
- Grases, A., Gracia, V., García-León, M., Lin-ye, J., & Sierra, J. P. (2020). Coastal flooding and erosion under a changing climate: Implications at a low-lying coast (ebro delta). *Water*, *12*(2), 1–26. <https://doi.org/10.3390/w12020346>
- Greenland, S., Senn, S. J., Rothman, K. J., Carlin, J. B., Poole, C., Goodman, S. N., & Altman, D. G. (2016). Statistical tests, P values, confidence intervals, and power: a guide to misinterpretations. *European Journal of Epidemiology*, *31*(4), 337–350. <https://doi.org/10.1007/s10654-016-0149-3>
- Hauser, L. T., Nguyen Vu, G., Nguyen, B. A., Dade, E., Nguyen, H. M., Nguyen, T. T. Q., ... Pham, H. V. (2017). Uncovering the spatio-temporal dynamics of land cover change and fragmentation of mangroves in the Ca Mau peninsula, Vietnam using multi-temporal SPOT satellite imagery (2004–2013). *Applied Geography*, *86*, 197–207. <https://doi.org/10.1016/j.apgeog.2017.06.019>
- Hayes, M. O. (1975). Morphology of Sand Accumulation in Estuaries: an Introduction To the Symposium. In *Geol and Eng* (Vol. 2). <https://doi.org/10.1016/b978-0-12-197502-9.50006-x>
- Himmelstoss, E. A., Henderson, R. E., Kratzmann, M. G., & Farris, A. S. (2018). *Digital Shoreline Analysis System (DSAS) Version 5.0 User Guide: U.S. Geological Survey Open-File Report 2018–1179*. Retrieved from <https://doi.org/10.3133/ofr20181179>
- Hoffmann, J. P. (2010). *Hoffmann: Linear regression analysis: Applications...* - Google Scholar (2nd ed.). Retrieved from [https://scholar.google.com/scholar\\_lookup?title=Linear regression analysis%3A applications and assumptions&publication\\_year=2010&author=Hoffmann%2CJP](https://scholar.google.com/scholar_lookup?title=Linear+regression+analysis%3A+applications+and+assumptions&publication_year=2010&author=Hoffmann%2CJP)
- Horton, B. P., Khan, N. S., Cahill, N., Lee, J. S. H., Kemp, A. C., Engelhart, S. E., ... Garner, A. J. (2020). Estimating global mean sea-level rise and its uncertainties by 2100 and 2300 from an expert survey. *Npj Climate and Atmospheric Science*, *3*(18), 1–8. <https://doi.org/10.1038/s41612-020-0121-5>
- Kalman, R. E. (1960). A new approach to linear filtering and prediction problems. *Journal of Fluids Engineering, Transactions of the ASME*, *82*(1), 35–45. <https://doi.org/10.1115/1.3662552>
- Kendall, M. G. (1975). *Rank correlation methods* (4th ed.). Retrieved from <https://www.worldcat.org/title/rank-correlation-methods/oclc/3827024>
- Kim, S., & Kim, H. (2016). A new metric of absolute percentage error for intermittent demand forecasts. *International Journal of Forecasting*, *32*(3), 669–679. <https://doi.org/10.1016/j.ijforecast.2015.12.003>
- Konko, Y., Bagaram, B., Julien, F., Akpamou, K. G., & Kokou, K. (2018). Multitemporal Analysis of Coastal Erosion Based on Multisource Satellite Images in the South of the Mono Transboundary Biosphere Reserve in Togo (West Africa). *Open Access Library Journal*, *05*(04), 1–21. <https://doi.org/10.4236/oalib.1104526>
- Kopp, R. E., Deconto, R. M., Bader, D. A., Hay, C. C., Radley, M., Kulp, S., ... Strauss, B. H. (2017). Evolving Understanding of Antarctic Ice-Sheet Physics and Ambiguity in Probabilistic Sea-Level Projections Earth ' s Future. *Earth's Future*. <https://doi.org/10.1002/2017EF000663>
- Leatherman, S. P. (2003). *Shoreline Change Mapping and Management Along the U . S . East Coast*. (38), 5–13. Retrieved from <https://www.jstor.org/stable/25736596>
- Lee, J., & Jurkevich, I. (1990). Coastline detection and tracing in SAR images. *IEEE Transactions on Geoscience and Remote Sensing*, *28*(4), 662–668. <https://doi.org/10.1109/TGRS.1990.572976>
- Lee, J. S., Jurkevich, I., Dewaele, P., Wambacq, P., & Oosterlinck, A. (1994). Speckle filtering of synthetic aperture radar images: a review. *Remote Sensing Reviews*, *8*(4), 313–340. <https://doi.org/10.1080/02757259409532206>
- Levy, J., Nolin, A., Fountain, A., & Head, J. (2014). Hyperspectral measurements of wet, dry and saline soils from the McMurdo Dry Valleys: Soil moisture properties from remote sensing. *Antarctic Science*, *26*(5), 565–572. <https://doi.org/10.1017/S0954102013000977>
- Liu, H., & Jezek, K. (2004a). A complete high-resolution coastline of antarctica extracted from orthorectified radarsat SAR imagery. *Photogrammetric Engineering and Remote Sensing*, *70*(5), 605–616. <https://doi.org/10.14358/PERS.70.5.605>
- Liu, H., & Jezek, K. C. (2004b). Automated extraction of coastline from satellite imagery by integrating Canny edge detection and locally adaptive thresholding methods. *Int. J. Remote Sensing*, *25*(5), 937–958. <https://doi.org/10.1080/0143116031000139890>
- Liu, Y., Li, J., Fasullo, J., & Galloway, D. L. (2020). Land subsidence contributions to relative sea level rise at tide gauge Galveston Pier 21 , Texas. *Scientific Reports*, *10*(17905), 1–11. <https://doi.org/10.1038/s41598-020-74696-4>
- Macqueen, J. (1967). Some methods for classification and analysis of multivariate observations. *Proc. of the*

- Fifth Berkeley Symposium on Mathematical Statistics and Probability*, 5.1, 281–297. Retrieved from <https://projecteuclid.org/euclid.bsmmsp/1200512992>
- Malinowski, R., Groom, G., Schwanghart, W., & Heckrath, G. (2015). Detection and delineation of localized flooding from WorldView-2 multispectral data. *Remote Sensing*, 7(11), 14853–14875. <https://doi.org/10.3390/rs71114853>
- Mann, H. B. (1945). Nonparametric Tests Against Trend. *Econometrica*, 13(3), 245. <https://doi.org/10.2307/1907187>
- McFeeters, S. K. (1996). The use of the Normalized Difference Water Index (NDWI) in the delineation of open water features. *International Journal of Remote Sensing*, 17(7), 1425–1432. <https://doi.org/10.1080/01431169608948714>
- Mirsane, H., Maghsoudi, Y., Emadi, R., & Mostafavi, M. (2018). Automatic Coastline Extraction Using Radar and Optical Satellite Imagery and Wavelet-IHS Fusion Method. *International Journal of Coastal and Offshore Engineering*, 2(2), 11–20. <https://doi.org/10.29252/ijcoe.2.2.11>
- Mukhopadhyay, A., Mukherjee, S., Mukherjee, S., Ghosh, S., Hazra, S., & Mitra, D. (2012). Automatic shoreline detection and future prediction: A case study on Puri coast, Bay of Bengal, India. *European Journal of Remote Sensing*, 45(1), 201–213. <https://doi.org/10.5721/EuJRS20124519>
- Nandi, S., Ghosh, M., Kundu, A., Dutta, D., & Baksi, M. (2016). Shoreline shifting and its prediction using remote sensing and GIS techniques: a case study of Sagar Island, West Bengal (India). *Journal of Coastal Conservation*, 20(1), 61–80. <https://doi.org/10.1007/s11852-015-0418-4>
- National Oceanography Centre. (2020). *Using Optical Satellite Shoreline Detection to measure historic and forecast future sandy shoreline changes in North Africa*. Southampton: World Bank.
- Oppenheimer, M., Glavovic, B. C., Hinkel, J., van de Wal, R., Magnan, A. K., Abd-Elgawad, A., ... Sebesvari, Z. (2019). *Sea Level Rise and Implications for Low Lying Islands, Coasts and Communities*. In: *IPCC Special Report on the Ocean and Cryosphere in a Changing Climate* (H. O. Pörtner, D. C. Roberts, V. Masson-Delmotte, P. Zhai, M. Tignor, E. Poloczanska, ... W. N.M., eds.). In press.
- Pajak, M. J., & Leatherman, S. (2002). The High Water Line as Shoreline Indicator. *Journal of Coastal Research*, 18(2), 329–337. Retrieved from <https://www.jstor.org/stable/4299078>
- Paravolidakis, V., Ragia, L., & Moirogiorgou, K. (2018). Automatic Coastline Extraction Using Edge Detection and Optimization Procedures. *Geosciences*, 8(407), 1–19. <https://doi.org/10.3390/geosciences8110407>
- Pardo-Pascual, J. E., Sánchez-García, E., Almonacid-Caballer, J., Palomar-Vázquez, J. M., de los Santos, E. P., Fernández-Sarría, A., & Balaguer-Beser, Á. (2018). Assessing the accuracy of automatically extracted shorelines on microtidal beaches from landsat 7, landsat 8 and sentinel-2 imagery. *Remote Sensing*, 10(2), 1–20. <https://doi.org/10.3390/rs10020326>
- Pollard, J. A. (2018). The interactive relationship between coastal erosion and flood risk. *Progress in Physical Geography*, 43(4), 574–585. <https://doi.org/10.1177/0309133318794498>
- Pradhan, B., Rizeci, H. M., & Abdulle, A. (2018). Quantitative Assessment for Detection and Monitoring of Coastline Dynamics with Temporal RADARSAT Images. *Remote Sensing*, 10(11), 1–18. <https://doi.org/10.3390/rs10111705>
- Rashmi, S., Addamani, S., & Ravikiran, S. (2014). Spectral Angle Mapper Algorithm for Remote Sensing Image Classification. *International Journal of Innovative Science, Engineering & Technology*, 1(4), 201–205. Retrieved from [http://ijiset.com/v1s4/IJISSET\\_V1\\_I4\\_27.pdf](http://ijiset.com/v1s4/IJISSET_V1_I4_27.pdf)
- Rumson, A. G., Hallett, S. H., & Brewer, T. R. (2017). Coastal risk adaptation: the potential role of accessible geospatial Big Data. *Marine Policy*, 83(June), 100–110. <https://doi.org/10.1016/j.marpol.2017.05.032>
- Ryabchuk, D., Spiridonov, M., Zhamoida, V., Nesterova, E., & Sergeev, A. (2012). Long term and short term coastal line changes of the Eastern Gulf of Finland. Problems of coastal erosion. *Journal of Coastal Conservation*, 16(3), 233–242. <https://doi.org/10.1007/s11852-010-0105-4>
- Sagne, P., Fall, B., Ba, K., Faye, G., Sow, E. H., & Niang, I. (2020). Impacts of the storm surges on sandy beaches: Example of northern coast of Dakar (Senegal). *EWASH & TI*, 4(1), 325–335. Retrieved from <https://revues.imist.ma/index.php/ewash-ti/article/download/19357/11035>
- Sane, M., & Yamagishi, H. (2004). Coastal Erosion in Dakar, Western Senegal. In *Jour. Japan Soc. Eng. Geol* (Vol. 44). <https://doi.org/10.5110/jjseg.44.360>
- Siswati, B. H., Mahanal, S., Susilo, H., & Corebima, A. D. (2016). Slope and intercept of regression equations of the correlation between metacognitive skill and concept gaining of the students having different academic capabilities in biology learning at senior high schools in Malang, Indonesia. *International Journal of Innovation and Research in Educational Sciences*, 3(2), 129–135.

- Stive, M. J. F., Aarninkhof, S. G. J., Hamm, L., Hanson, H., Larson, M., Wijnberg, K. M., ... Capobianco, M. (2002). Variability of shore and shoreline evolution. *Coastal Engineering*, 47, 211–235. [https://doi.org/https://doi.org/10.1016/S0378-3839\(02\)00126-6](https://doi.org/https://doi.org/10.1016/S0378-3839(02)00126-6)
- Storey, J., Roy, D. P., Masek, J., Gascon, F., Dwyer, J., & Choate, M. (2016). A note on the temporary misregistration of Landsat-8 Operational Land Imager (OLI) and Sentinel-2 Multi Spectral Instrument (MSI) imagery. *Remote Sensing of Environment*, 186, 121–122. <https://doi.org/10.1016/j.rse.2016.08.025>
- Stronkhorst, J., Huisman, B., Giardino, A., Santinelli, G., & Santos, F. D. (2018). Sand nourishment strategies to mitigate coastal erosion and sea level rise at the coasts of Holland (The Netherlands) and Aveiro (Portugal) in the 21st century. *Ocean and Coastal Management*, 156(February 2017), 266–276. <https://doi.org/10.1016/j.ocecoaman.2017.11.017>
- Su, L., & Gibeaut, J. (2017). Using UAS Hyperspatial RGB Imagery for Identifying Beach Zones along the South Texas Coast. *Remote Sensing*, 9(159), 1–14. <https://doi.org/10.3390/rs9020159>
- Taylor, R. (1990). Interpretation of the Correlation Coefficient: A Basic Review. *Journal of Diagnostic Medical Sonography*, Vol. 6, pp. 35–39. <https://doi.org/10.1177/875647939000600106>
- Thior, M., Sané, T., Dièye, E. hadj B., Sy, O., Cissokho, D., Ba, B. D., & Descroix, L. (2019). Coastline dynamics of the northern Lower Casamance (Senegal) and southern Gambia littoral from 1968 to 2017. *Journal of African Earth Sciences*, 160, 103611. <https://doi.org/10.1016/j.jafrearsci.2019.103611>
- Thoai, D. T., Dang, A. N., & Kim Oanh, N. T. (2019). Analysis of coastline change in relation to meteorological conditions and human activities in Ca mau cape, Viet Nam. *Ocean and Coastal Management*, 171(October 2018), 56–65. <https://doi.org/10.1016/j.ocecoaman.2019.01.007>
- Toure, S., Diop, O., Kpalma, K., & Maiga, A. S. (2018). Coastline detection using Fusion of Over Segmentation and Distance Regularization Level Set Evolution. *International Archives of the Photogrammetry, Remote Sensing and Spatial Information Sciences - ISPRS Archives*, 42(3W4), 513–518. <https://doi.org/10.5194/isprs-archives-XLII-3-W4-513-2018>
- Toure, S., Diop, O., Kpalma, K., & Maiga, A. S. (2019). Shoreline detection using optical remote sensing: A review. *ISPRS International Journal of Geo-Information*, 8(2), 1–21. <https://doi.org/10.3390/ijgi8020075>
- Tu, T. M., Su, S. C., Shyu, H. C., & Huang, P. S. (2001). A new look at IHS-like image fusion methods. *Information Fusion*, 2(3), 177–186. [https://doi.org/10.1016/S1566-2535\(01\)00036-7](https://doi.org/10.1016/S1566-2535(01)00036-7)
- van der Werff, H. M. A. (2019). Mapping shoreline indicators on a sandy beach with supervised edge detection of soil moisture differences. *Int. J. Appl Earth Obs Geoinformation*, 74, 231–238. <https://doi.org/10.1016/j.jag.2018.09.007>
- Vos, K., Splinter, K. D., Harley, M. D., Simmons, J. A., & Turner, I. L. (2019). CoastSat: A Google Earth Engine-enabled Python toolkit to extract shorelines from publicly available satellite imagery. *Environmental Modelling and Software*, 122. <https://doi.org/10.1016/j.envsoft.2019.104528>
- Wahl, T., Jensen, J., Frank, T., & Haigh, I. D. (2011). Improved estimates of mean sea level changes in the German Bight over the last 166 years. *Ocean Dynamics*, 61(5), 701–715. <https://doi.org/10.1007/s10236-011-0383-x>
- Wang, F., Shao, W., Yu, H., Kan, G., He, X., Zhang, D., ... Wang, G. (2020). Re-evaluation of the Power of the Mann-Kendall Test for Detecting Monotonic Trends in Hydrometeorological Time Series. *Frontiers in Earth Science*, 8(February), 1–12. <https://doi.org/10.3389/feart.2020.00014>
- Wong, T. E., Bakker, A. M. R., & Keller, K. (2017). *Impacts of Antarctic fast dynamics on sea-level projections and coastal flood defense*. 347–364. <https://doi.org/10.1007/s10584-017-2039-4>
- Wright, L. D., & Short, A. D. (1984). Morphodynamic variability of surf zones and beaches: A synthesis. *Marine Geology*, 56(1–4), 93–118. [https://doi.org/10.1016/0025-3227\(84\)90008-2](https://doi.org/10.1016/0025-3227(84)90008-2)
- Xu, H. (2006). Modification of normalised difference water index (NDWI) to enhance open water features in remotely sensed imagery. *International Journal of Remote Sensing*, 27(14), 3025–3033. <https://doi.org/10.1080/01431160600589179>
- Yu, S., Mou, Y., Xu, D., You, X., Zhou, L., & Zeng, W. (2013). A New Algorithm for Shoreline Extraction from Satellite Imagery with Non-Separable Wavelet and Level Set Method. *International Journal of Machine Learning and Computing*, 3(1), 158–163. <https://doi.org/10.7763/IJMLC.2013.V3.293>
- Yue, S., Pilon, P., & Phinney, B. (2003). Canadian streamflow trend detection: Impacts of serial and cross-correlation. *Hydrological Sciences Journal*, 48(1), 51–63. <https://doi.org/10.1623/hysj.48.1.51.43478>
- Yue, S., & Wang, C. Y. (2004). The Mann-Kendall Test Modified by Effective Sample Size to Detect Trend in Serially Correlated Hydrological Series. *Water Resources Management*, 18, 201–218.

- <https://doi.org/https://doi.org/10.1023/B:WARM.0000043140.61082.60>
- Zhang, T., Yang, X., Hu, S., & Su, F. (2013). Extraction of Coastline in Aquaculture Coast from Multispectral Remote Sensing Images: Object-Based Region Growing Integrating Edge Detection. *Remote Sensing*, 5, 4470–4487. <https://doi.org/10.3390/rs5094470>
- Zheng, X., Lei, Q., Yao, R., Gong, Y., & Yin, Q. (2018). Image segmentation based on adaptive K -means algorithm. *EURASIP Journal on Image and Video Processing*, 2018(68). <https://doi.org/https://doi.org/10.1186/s13640-018-0309-3>
- Zhou, H., Deng, Z., Xia, Y., & Fu, M. (2016). A new sampling method in particle filter based on Pearson correlation coefficient. *Neurocomputing*, 216, 208–215. <https://doi.org/10.1016/j.neucom.2016.07.036>



